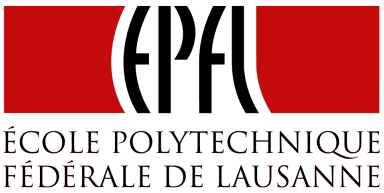

SHPM imaging of $LiHoF_4$ at ultra low temperatures.

Master Thesis

Supervised by:

Professor Henrik M. Ronnow

and

Dr. Julian O. Piatek

Laboratory for quantum magnetism (LQM)

Faculté des Sciences de base
de
l'Ecole Polytechnique Fédérale de Lausanne (EPFL)

Presented by

Pau Jorba

Master Student in Physics
at EPFL

LAUSANNE
January 2014

II

Abstract

In the first part of this thesis we describe the functioning principle of the scanning hall probe microscope (SHPM), and we present a summary of the theoretical and experimental knowledge on the dipolar-coupled Ising ferromagnet $LiHoF_4$. In the second chapter we present the experimental setup that allows us to perform SHPM imaging at ultra low temperatures. The main components; microscope head, dilution refrigerator (DR), and vibration-free cryostat, are described in detail. We also explain the choice of samples geometries used, and the surface preparation performed. Some modifications made to the microscope to enhance its performance are also detailed.

The experimental results are separated into two chapters, the first with more qualitative observations, and the second one where we attempt to extract quantitative information from the images. We present different sets of SHPM images taken on different sample geometries, with two sample orientations (a-a and a-c planes), at different temperatures (from 20 mK to 1.6 K), and under transverse magnetic fields up to 3 Tesla. In the first chapter we discuss the ground state domain structure and how the order parameters perturb it. In the second chapter we attempt to extract a detailed domain structure by a rudimentary image treatment. We also describe the change in magnetization with temperature, and compare it with other experimental data.

Abreviations: Scanning Hall Probe Microscope (SHPM), Dilution Refrigerator (DR), Scanning Tunneling Microscope (STM), Hall Probe (HP), Room Temperature (RT), Inner Vacuum Chamber (IVC), Mixing Chamber (MC), Oxygen Free High Conductivity copper (OFHC copper).

Contents

Chapter 1

Introduction

1.1 SHPM principle

In 1981 Gerd Binning and Heinrich Rohrer develop the first scanning tunneling microscope (STM), which earned them the Nobel Prize in Physics in 1986. This technique is based on the quantum tunneling of electrons from the microscope tip to a conducting surface, and the use of a piezoelectric ceramic scanner to control the tip position with very high precision. The tunneling current changes exponentially with the height z of the tip as: $J_T \propto exp(-\alpha z)$, where α depends on the material [1]. The so-called STM feedback, actively changes the voltage on the piezoelectric responsible of the vertical movement to keep a constant tunneling current. Scanning a material at a constant tunneling current, implies a constant distance z from the surface, so by recording the displacement of the tip we get the topographic information. This technique allowed unprecedented microscope resolution (currently atomic resolution), but also opened to door to the development of many other techniques based on a similar design. For example, the atomic force microscope, developed in 1986, uses the interaction force between the tip and the sample.

The scanning Hall probe microscope (SHPM) was first developed in 1992. This technique combines the precision positioning of the STM, with a nano-fabricated semiconductor Hall sensor, to give images of sub-micron precision, and outstanding magnetic field sensitivity [2]. Compared to other techniques which image magnetic surfaces, SHPM has a good combination of high spatial resolution, a quantitative measure of the magnetic field, and non-invasiveness. The current development of this technique, is focused on a more accurate spatial resolution, and wider accessible temperature range (30 mK - 300 K). As we decrease the size of the Hall sensor (usually a 2D electron gas) to increase the resolution, the resistance increases resulting in more noise, and at very low temperatures ($< 4K$), the charge carriers may deplete, making the Hall sensor useless.

As seen in figure 1.1, our Hall probe (HP) incorporates a gold coated tip for STM feedback. The hall probe is of 1 square micron size and it is placed at about 7 microns from the STM tip. One can easily see the four contacts that necessary for a Hall measurement. The HP is tilted about 1 degree respect to the sample, ensuring that the tip is the closest point. In figure 1.2 we present a schematic describing the functioning principle of the SHPM. The high precision electronics drive the piezoelectrics to scan the surface with the HP, while the

STM feedback ensures that the HP doesn't crash on the surface. During this process the Hall signal is recorded. The positioning information and the Hall signal are combined together by the software to create an image.

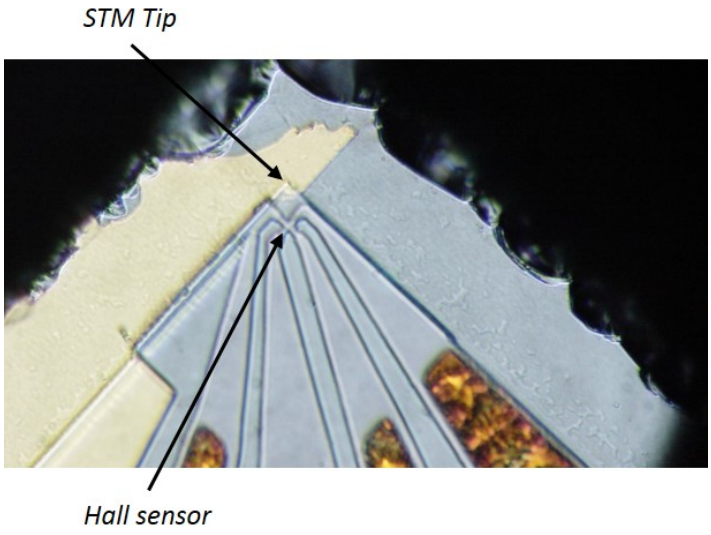

Figure 1.1: Picture of the HP used during this study.

The microscope can be run in two modes, STM tracking, and lift-mode. The first mode uses the STM feedback to measure simultaneously topographic and magnetic information. With this method, the hall probe is closer to the surface (about 100 nm) and gives a slightly better resolution. The disadvantage of this mode is that it needs very flat surfaces to work properly. The tip is also very large compared to conventional STM tips, so the topography will have a poor resolution. Also, in order to reduce the risk of crashing the HP on the surface, the scanning across the surface is done slowly. Finally, the magnetic information is taken few microns away from the position of the tip, so there is a strong spatial shift between them.

In lift-mode, the STM feedback is only used to locate the surface. The HP is lifted at a certain distance of the surface, and the image is taken at a constant height. Due to the inclination of the surface, and for a standard frame of 12×12 microns, this distance usually varies from 200 to 500 nanometers. For our experiments, given the size of our Hall sensor ($1\mu m^2$), the lift-mode gives similar resolution to the STM tracking mode. As it is a safer and faster method, it has been the most used technique for the SHPM images.

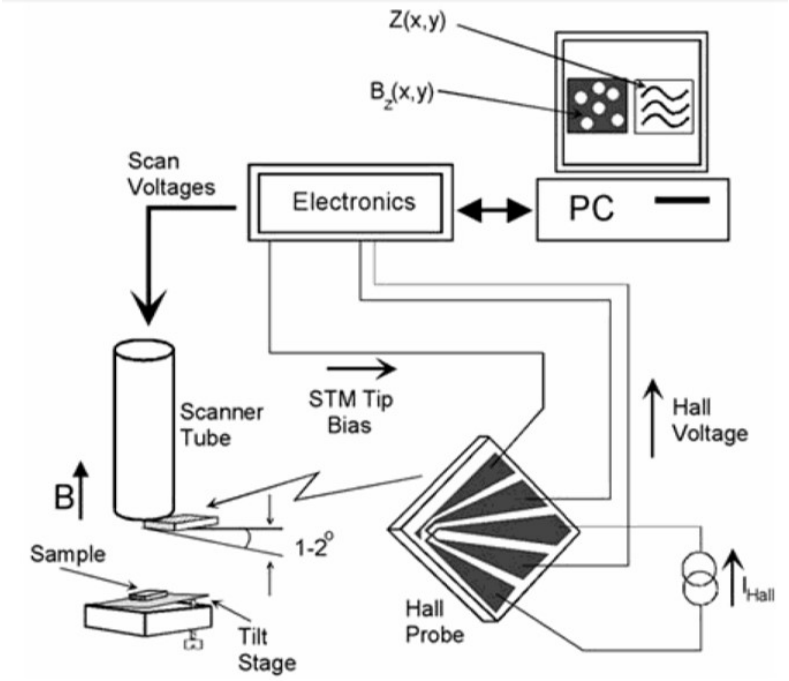

Figure 1.2: Schematic of the functioning principle of our SHPM.

1.2 LiHoF$_4$ an Ising dipolar magnet

In this thesis we study the rare earth compound $LiHoF_4$. It is a very well characterized dipolar-coupled Ising ferromagnet, that has been studied for almost the past 40 years [3]. Besides the classical, thermally driven, phase transition from a ferromagnetic state to a paramagnetic state ($T_c = 1.53$ K), it presents a quantum phase transition at zero temperature driven by a transverse magnetic field ($H_c^t = 5$ T) [4]. The special interest in $LiHoF_4$ is because it presents interesting physical phenomena, and at the same time, is a system with a relatively simple and well characterized Hamiltonian. It is a nice playground for testing theoretical predictions and quantum effects in many-body systems. It is possible to grow big single crystals with very few defects.

The crystal structure of LiReF$_4$ compounds is presented in the figure 1.3. It is a tetragonal structure where each of the rare-earth ions occupies a position with S4 symmetry, and is surrounded by 8 fluorine ions, which generate the local crystal field environment. In the specific case of $LiHoF_4$, where this position is occupied by a Ho^{3+} ion, the unit cell size is (1,1,2.077) in units of $a = 5.175$ Å. According to Hund's rule, the holmium ion has a degenerate ground state, but the crystal field breaks the degeneracy, to a doublet ground state with only a c component, separated from the first excited state by 11 K [3]. When we are at very low temperatures, the Ho ions can be represented by the $\sigma^z = \pm 1$ Ising states, due to the strong anisotropy generated by the crystal field.

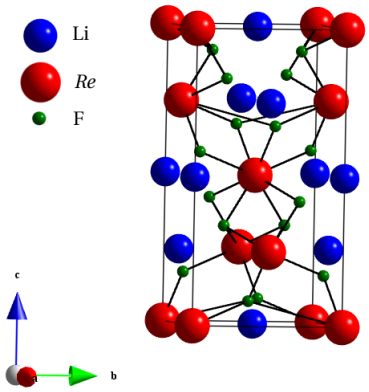

Figure 1.3: Diagram showing the tetragonal crystal structure of the LiReF$_4$ system. Red spheres are rare-earth ions (in our chase Ho^{3+} ions), blue are lithium, and green are fluorine. The black bonds indicate the fluorine ions which contribute to the crystal field around the rare-earth ions. (Taken from [5])

The total Hamiltonian includes, in order, the crystal field, the hyperfine, the Zeeman, and the classical dipole-dipole interactions. Finally, the nearest-neighbor Heisenberg exchange interaction is included:

$$\mathcal{H} = \sum_i [H_{CF}(\mathbf{J}_i) + \mathcal{A}\mathbf{J}_i \cdot \mathbf{I}_i - g\mu_B \mathbf{J}_i \cdot \mathbf{H}] - \frac{1}{2}\sum_{ij}\sum_{\alpha\beta} \mathcal{J}_D D_{\alpha\beta}(ij)\mathbf{J}_{i\alpha}\mathbf{J}_{j\beta} - \frac{1}{2}\sum_{ij}^{n.n} \mathcal{J}_{12}\mathbf{J}_i \cdot \mathbf{J}_j, \quad (1.1)$$

where H_{CF} is the crystal field, $\mathcal{A}$ is the hyperfine coupling, $\mathbf{J}_i$ and $\mathbf{I}_i$ are respectively the electronic angular momentum and the nuclear spin of the i^{th} ion, $\mathcal{J}_\mathcal{D}$ is the dipole coupling, $D_{\alpha\beta}(ij)$ is the classical dipole tensor and $\mathcal{J}_{12}$ is the exchange coupling [3].

As we mentioned, the crystal field is responsible for modifying the electronic configuration. When the symmetry of the crystal is taken in account, only six parameters need to be determined. The hyperfine coupling between the electronic moments and the spin $\mathbf{I} = 7/2$ cause a small splitting of each crystal field level. This splitting has strong effects near the quantum critical point, but is of small interest for the present discussion. For the Zeeman energy, the Landé factor is $g = 5/4$, and μ_B is the Bohr magneton. The normalized dipole tensor $D_{\alpha\beta}(ij)$ is directly calculable, and the dipole coupling strength $\mathcal{J}_D = 1.1654\ \mu eV$, is simply fixed by lattice constants. The exchange constant can be determined by fitting experimental data, it happens to be very weak $\mathcal{J}_{12} = -0.1\ \mu eV$ compared with the dipolar coupling [6].

Given those arguments, the Hamiltoninan can be simplified into the $S = 1/2$ model of an Ising magnet in a transverse magnetic field. The corresponding Hamiltonian is:

$$\mathcal{H} = \sum_{ij} \mathcal{J}_{ij}\sigma_i^z\sigma_j^z - \Gamma\sum_i \sigma_j^x, \quad (1.2)$$

where $\mathcal{J}_{ij}$ are longitudinal couplings, σ are the Pauli spin matrices, and Γ is the transverse

field.

A detailed comparison of theory, experiments, and simulations is possible. Bitko *et. al.* demonstrates that the mean-field treatment of the full Hamiltonian, using the known crystal field and including nuclear hyperfine terms, accurately matches experiment [4]. In the figure 1.4 we present the experimental phase diagram of $LiHoF_4$ compared to theoretical mean-field treatment. Refinement of mean-field treatment has been performed to better match the magnetic excitations near the quantum phase transition [6]. They suggest that the slight mismatch between theory and experiments, could be better understood in terms of the domain walls dynamics and shape effects. More recently, simulations on $LiHoF_4$ where able to give evidence of the logarithmic corrections predicted in renormalization group theory.

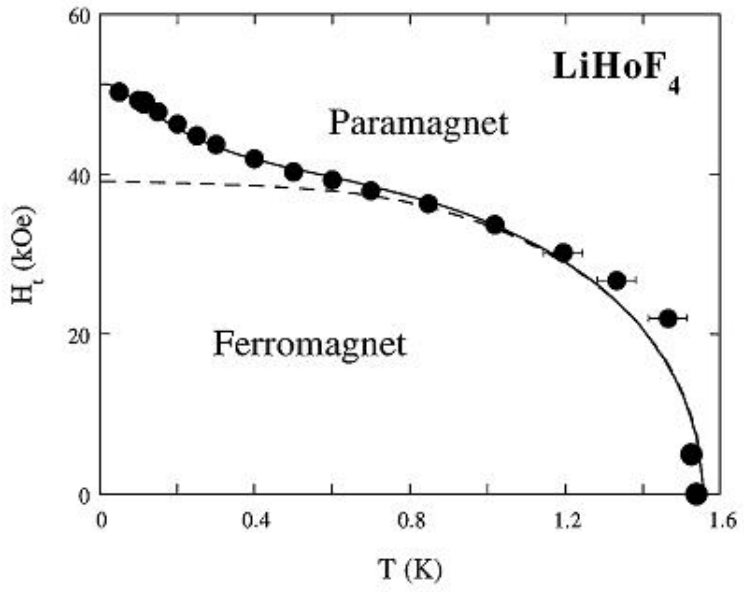

Figure 1.4: Experimental AC susceptibility phase boundary (filled circles) of the ferromagnetic transition in the transverse field-temperature plane. Dashed line is a mean-field theory including only the electronic degrees of freedom, solid line is a full mean field theory incorporating the nuclear hyperfine interaction. (Taken from [4])

Despite the great theoretical understanding, the exact domain structure of $LiHoF_4$ seems to be controversial. The theoretical studies on Ising dipolar magnets suggest a domain structure of parallel sheets of opposite magnetization [7] [8] [9]. Special attention is given to the branched state (Figure 1.5) which is believed to present a rich variety of behavior as function of temperature and field. This process mostly affects the surface of the sample, in order to effectively reduce the magnetostatic energy, by creating smaller spike-like domains of opposite magnetization inside a domain. Experimental data on the domain structure of $LiHoF_4$ existing in literature is of very bad quality [10], or of poor resolution and limited minimum temperature (1.3 K) [11]. At this moment there is not a demonstrated theory for the magnetic domains.

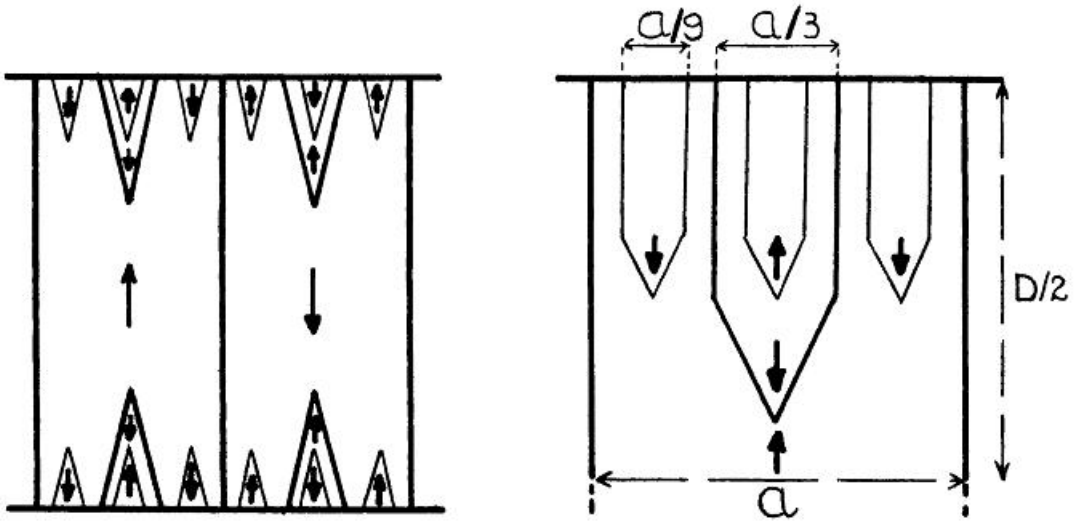

Figure 1.5: Representation of a doubly branched state for a period of the structure (left). A doubly branched state in a different model for half period (right). (Taken from [9])

The interest in the magnetic domains of $LiHoF_4$ is not purely theoretical, as it can be understood from the above discussions. The use of magnetic materials from information storage to power conversion depends crucially on its domain structure. Silevitch *et. al.* show that a transverse magnetic field applied to the doped compound $LiHo_xY_{1-x}F_4$ is an isothermal regulator of domain pinning [12]. They claim that the principles discovered for the rare-earth compounds at cryogenic temperatures are general, and could be implemented in highly anisotropic ferromagnets with ordering at room temperature. A more complex experimental realization is related with quantum computing. By experimenting on the quantum annealing of $LiHo_xY_{1-x}F_4$ Brooke *et. al.* speculate about the realization of a low refined quantum computer, where the computation is solved by a thermal cooling and the application of a transverse field, the result information would be hold by the resulting spin configuration, as a set of ones and zero values [13]. It would then be interesting to understand in which way we can influence the frozen spin configuration (at very low temperature) of $LiHoF_4$ by means of temperature and transverse field.

Chapter 2

Experimental details

2.1 Experimental setup

Our experimental setup is divided into 5 main parts. First, the microscope head, which for our experiment, is the most interesting element. Then the dilution refrigerator (DR), where the microscope head is mounted, and that is responsible for achieving the temperature range that we need for our experiment. Another important element is the cryostat, it is necessary to run the DR, and it allows us to run a superconducting magnet. The vibrational insulation, which is critical for SPM measurements, takes place at the level of the cryostat. Finally, the control of the microscope is ensured by high precision electronics.

2.1.1 Microscope head

The SHPM was provided by *Nanomagnetics Instruments* and adapted to fit on the Kelvinox-400 DR insert from *Oxford Instruments*. Its cylindrical design is ideal for low temperature and high magnetic field applications. The outer diameter of the head is less than 30 millimeters, it can easily fit in a superconducting magnet. In the figure 2.1, one can see a picture of the SHPM head after an experiment. There are indications on the different components which will be explained in detail.

This microscope has to be mounted and tested at room temperature (RT), and then cooled down to cryogenic temperatures. There is an important thermal expansion across this huge range of temperatures that has to be taken in account. First, the separation between the sample and the HP might increase or decrease considerably, which could eventually crash the HP on the sample. In our case, we know that the sample gets closer to the HP as one warms up the system. Furthermore, the behavior of the piezoelectric materials changes with temperature as the thermal expansion induces changes in the anion-cation bonds (which is why they are also known as pyroelectric materials). The main consequence of this second effect is the decreasing of the scan range with decreasing temperature in the 3 directions of space, for the same voltage difference we have a smaller displacement. For this setup, at liquid helium temperature one can get an image up to 12×12 μm, whereas it would be of 100×100 μm at RT. In the z-direction we go from about 10 micron range at RT to 1 micron range at liquid helium temperatures. There is a built-in function in the software to take this in account. One can enter the temperature of work and using calibrated coefficients, the voltage applied to the piezos is translated into the appropriate displacement. From our experiments, we can tell

that in the temperature range that interest us (1.6 to 0.02 Kelvin), the piezoelectric behavior doesn't change significantly, as the features doesn't change size with temperature. This temperature behavior is also observed in a STM scanner used at ultra low temperatures [14].

To overcome some of these difficulties, the coarse movements along the z-direction are done via a sliding mechanism. in the figure 2.1 we present a picture of the SHPM head with indications of its components. The sample puck, where the sample is mounted, is attached with a leaf spring on to the quartz tube. The screws on the leaf spring are tightened enough that the sample puck cannot slide by itself on the quartz tube. By applying saw-tooth sloped electrical pulses on the slider piezoelectric, the puck moves closer or farther through slich-slip motion. One can then approach or remove the sample form the surface over a large distance by applying several pulses. Again, the thermal expansion makes the pulses much more effective at RT than at cryogenic temperatures, the ratio in distance per pulse is also around 10. The distance per step when approaching the surface at 25 mK was estimated to be about 300 nanometers. Moreover, when the experiment takes place, the microscope is in a vertical position, so the sample puck has to overcome its weight to approach the surface. In this situation, the approaching steps ($\sim 300\ nm$) are less effective than the retracting ones ($\sim 450\ nm$).

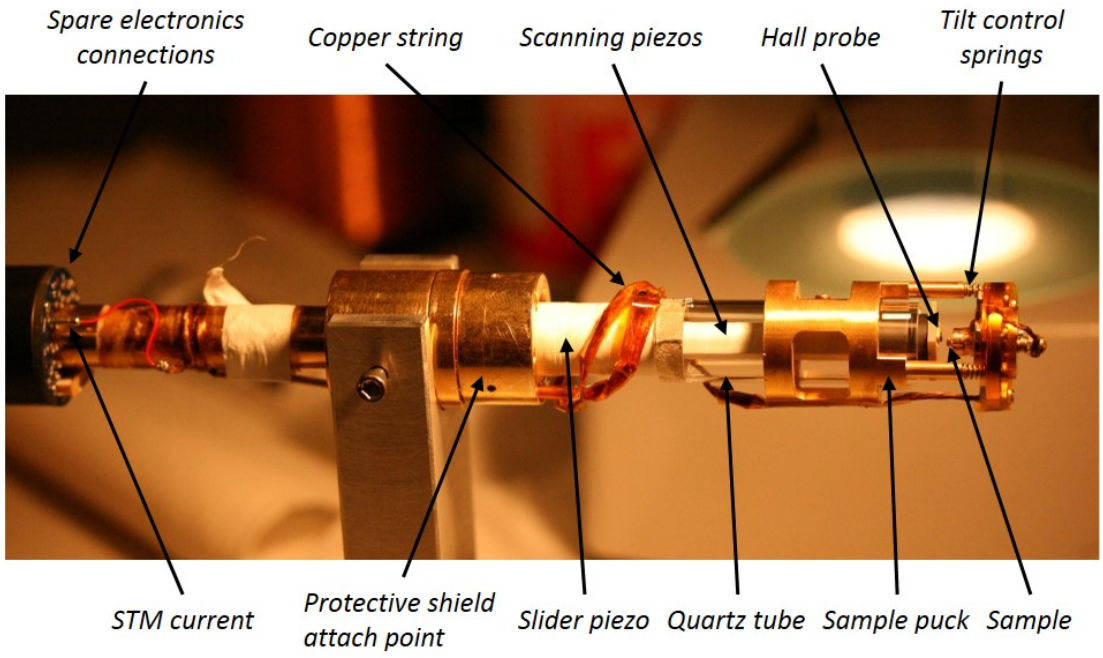

Figure 2.1: Picture of the SHPM head with indications.

The sample puck has 3 spring-loaded screws that allow us to tilt the sample with respect to the HP. It is made entirely from brass so it can conduct the STM current through it. To maintain the voltage bias between the STM tip and the sample, the sample puck has to be well insulated from the rest of the microscope, as the tip is grounded to the shield. An insulated wire is connected between the sample puck and "STM current connection" (*i.e.*

where the bias voltage is applied) to carry the tunneling current. As the quartz tube is also an insulator, the sample and the tip should be perfectly decoupled ($> 2M\Omega$). One can short circuit the sample puck and the microscope to see that the bias voltage cannot be maintained as a well functioning check before cooling the microscope. It has to be pointed out that, when applying a hall voltage at RT, we can get a significant leakage current to the STM tip. At RT, due to thermal excitation the material that insulates the Hall sensor from the STM tip has enough carriers to conduct a current, when cooling down the system this carriers are more and more depleted as the thermal energy decreases. Finally a protective metallic shield is fixed around the scanning space and the sample puck to protect it from mechanical shocks when mounting it on the fridge.

2.1.2 Dilution Refrigerator

To achieve the working temperatures, we use a dilution refrigerator. This instrument not only provides very low temperatures (milikelvin range), but also runs in continuous operation, this way one can keep the system at a certain temperature for very long time. It also provides a relatively large cooling power (400 μW at 100 mK), which can compensate the heating produced by the scanning mechanism.

The DR is based on utilizing the unique properties of mixtures of helium 3 (^{3}He boiling point: 3.19 K) and helium 4 (^{4}He boiling point: 4.2 K). Below a certain temperature (about 800 mK) there is a phase separation in the mixture. In the mixing chamber, where the lowest temperature is achieved, there are two phases coexisting, one which is very rich in ^{3}He and one which is mainly superfluid ^{4}He. The concentrated phase (rich in ^{3}He) is lighter than the other one and stays on the top. Taking a ^{3}He atom from the concentrated phase to the superfluid phase is an endothermic process. Since this phase separation exists at any temperature below 800 mK we are theoretically always able to remove heat from the medium. By pumping the ^{3}He through the superfluid ^{4}He we may maintain the low concentration of ^{3}He in the ^{4}He phase. [16].

A picture and a Schematic of the fridge are given in figure 2.2. The whole process is quite sophisticated, there are many commercially available dilution refrigerators in different configurations. In our case, the refrigerator is a Kelvinox 400 from *Oxfrod Instruments* (left of Figure 2.2), and it is operated inside a cryostat (also from *Oxfrod Instruments*). The cold part of the fridge (< 4 K) is in the inner vacuum chamber (IVC) which is in contact with the liquid helium of the cryostat. The top part of the fridge consists in a *1K pot* which evaporates liquid helium taken from the cryostat, by pumping on it we can get down to temperatures close to 1.5 K. The mixture enters the fridge through the condensing line where it is well thermalised with the 1K pot, and is liquefied. It is then driven down, through heat exchangers for further cooling, to the mixing chamber (MC) where the cooling process takes place with the phase separation mentioned above. Osmotic gradient pressure drives the flow of the dilute phase up through the heat exchanger and into the still where it is pumped. The circuit is closed, so once the mixture is pumped from the still, it is driven back to the condensing line. There is a gradient of temperature from the top of the IVC (4.2 K) to the bottom (base temperature around 7 mK), it is then important to have a proper insulation. The IVC is in high vacuum and there is a radiation shield thermalised to the cold plate (50mK at base temperature) protecting the MC plate and the sample space from the 4.2 K black body radiation of the

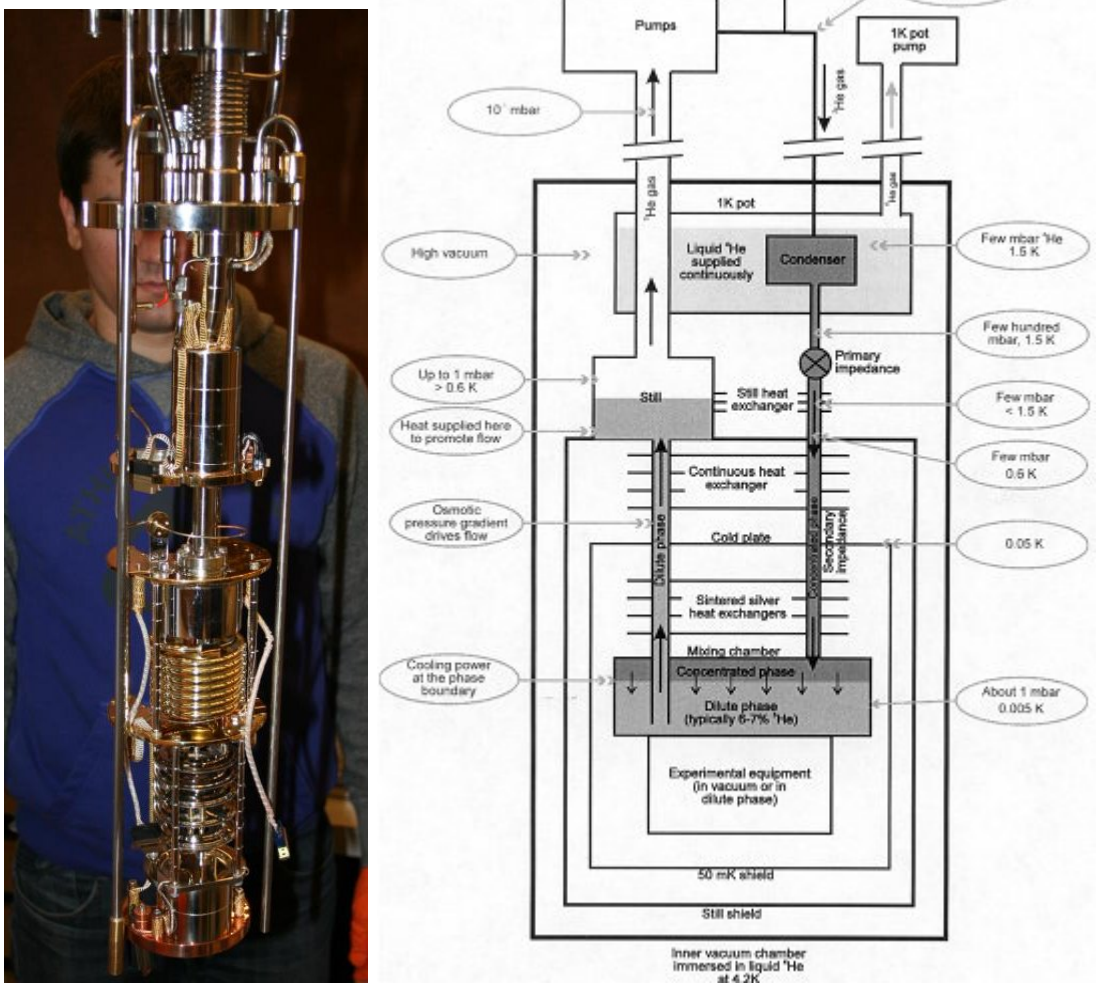

Figure 2.2: Picture of the inner part of our DR taken in the LQM lab (left). Schematic diagram of a dilution refrigerator (right) (taken from [15]).

IVC walls. The cooling power and the base temperature are directly related to the flow of the ^{3}He through the system. To improve it, it is important to have a powerful pump that it is able to pump the mixture at a high rate. Finally it is also important to ensure that there will be no contamination gases entering the fridge as they would freeze and block the lines. To avoid contamination, the mixture passes through liquid Nitrogen and liquid Helium cold traps before entering the condensing line.

The microscope is mounted underneath the MC. Once the fridge is closed, the head is inside the IVC and the radiation shield, the experiment takes place in high vacuum. When the fridge is lowered into the cryostat, the sample position is in the center of the superconducting magnet, allowing for a magnetic field to be applied on the sample during an image acquisition. An insert was specially designed to adapt the microscope head to the fridge and run the electrical connections from the top of the fridge to the head. Without this insert, a

base temperature of 8 mK is achieved, but due to extra heat load through the insert, this increases to 20 mK. One could possibly get a lower temperature by enhancing the thermal contact between the wires and the different stages of the fridge along the insert.

2.1.3 Cryostat and vibration damping

We run the DR in a cryostat from *Oxford Instruments* with a superconducting electromagnet that can reach magnetic fields up to 9 Tesla. The cryostat is suspended at three opposite points from pneumatic vibration isolators from *Newport* (model *S-2000 Stabilizer*) with automatic re-leveling (Figure 2.3). This stage should damp all possible high-frequency vibrations coming from the floor.

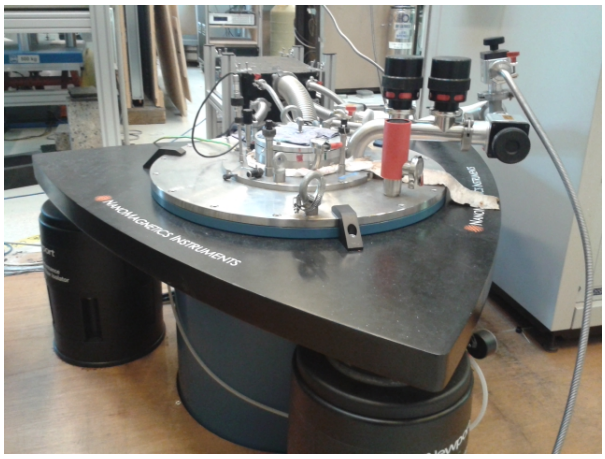

Figure 2.3: Picture of the cryostat suspended from the pneumatic vibration isolators.

All the tubes that are attached to the DR and the cryostat to ensure its proper functioning carry vibrations to the system, either actively because they are attached to a vibration source, or passively transmitting vibrations by contact. For example, the *1K pot* is pumped via a mechanical pump that produces huge vibrations. The system that pumps out the mixture is also susceptible to induce vibrations. To avoid this problem, all the tubes goes through a concrete block, that is supposed to damp most high-frequency vibrations (Figure 2.4). The block was fixed to the floor to enhance the damping.

There are few vibration issues that are not solved. For instance, the concrete block is not heavy enough, some vibrations can still pass through. Also, all the electronic cables that are connected to the fridge are susceptible to carry vibrations. Fortunately, our SPM system is neither designed, nor used, for atomic precision imaging, so small vibrations are acceptable. We have a vibration damping level that allow us to take high quality images. The only limitation we found was whenever there where vibrations into the helium recovery system. When the other cryostat in the lab have a high boiling rate (filling, lowering a fridge, etc), it creates strong vibrations that are carried to our cryostat by the helium. In this situation, the tunneling current on the surface is very unstable, and images get noisy. A gas damping system should be implemented if one wants to use the SHPM in this situation.

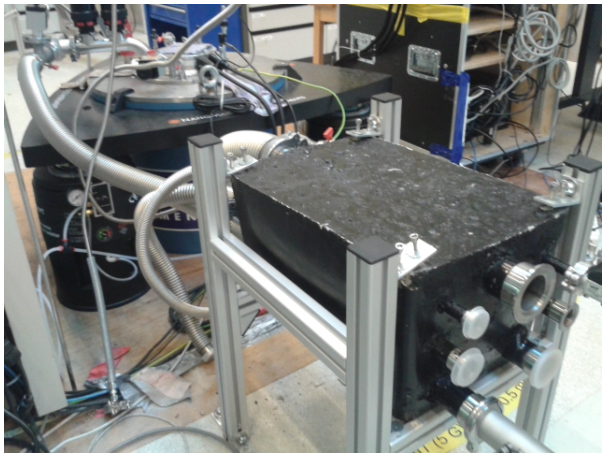

Figure 2.4: Picture of the concrete block, tubes of different diameter go straight through, flexible tubes can be attached in both sides.

2.2 Sample preparation

Our samples are $LiHoF_4$ single crystals. It is a relatively hard material. To get the desired shape and orientation, we use the usual technique, we mount the sample on a goniometer, we align it with a x-ray *LAUE* diffractometer, and with a diamond saw we cut into the desired geometry. We studied 3 different cuboids with increasing height-to-surface ratio. The first sample (flat sample) has an almost square surface of about 9×9 millimeters, with a height of 2.3 millimeters. The two big surfaces are parallel to each other, and perpendicular to the c-axis of the crystal. Its height-to-surface ratio is of 0.25 approximately. The second sample (cubic sample) has a rectangular surface of 1.5×2 millimeters, and a height of 1.7 millimeters. It is not a rectangular cuboid, as it is a small sample, one of the sides of the cuboid cracked during the cutting procedure giving an inclined face. Nevertheless, what matters is that the top and bottom surfaces are perpendicular to the c-axis of the crystal. We get a height-to-surface ratio of about 1. This sample was also used to image the a-c plane surface, so two opposite lateral faces where also cut along a crystallographic plane. The last sample (long sample), is an almost needle shaped sample with a square surface of 1.2×1.2 millimeters, and a height of 5 millimeters. It has a big height-to-surface ratio, almost 4.2. All the surfaces that were imaged, were polished carefully, paying special attention to keep the parallelism between top and bottom surfaces (*i.e.* keeping the imaged surface perpendicular to crystallographic axis). We used polishing paper for the coarse polishing, and then different polishing preparations with decreasing grain size. In the last polishing step, we used 50 nanometers grain size. This gives us, to within 100 nm, smooth enough surfaces for our purpose.

To ensure a proper STM feedback we need to have a good electrical contact between the sample surface and the sample puck. As $LiHoF_4$ is a highly insulating sample, one need to gold coat it. We found *gold sputtering* as the most appropriate technique. On all the samples but one, we deposited a layer between 80 and 100 nanometers of gold by *gold sputtering*. On the cubic sample we tried to deposit a thinner layer (20 nanometers), using *chemical vapor deposition* (CVD) under high vacuum. The result was a almost transparent layer. We are

not sure if it is due to its thickness, or the technique itself, but with sputtering one gets much stable tunneling currents. The coating done by CVD seemed to have been slightly removed by the imaging process, whereas with sputtering it seemed to be perfect after every experiment. Both techniques are almost unidirectional (*i.e.* the gold is not deposited on the lateral surfaces), the electrical contact from the surface to the sample holder is achieved using silver paint. The same paint is used to glue the sample on the sample holder.

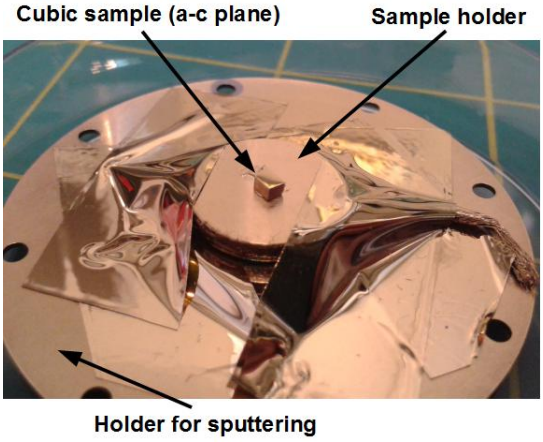

Figure 2.5: Picture of the cubic sample after gold coating the a-c plane surface. The sample was previously attached on the sample holder with silver paste.

Once the sample is ready for the SHPM one has to mount it properly on the sample puck. As described in the introduction, the HP has to have a slight tilt (1-1.4°) compared to the sample surface, ensuring the STM tip is the point closest to the sample. To do so, first the sample puck has to be rotated to align one of its legs with the symmetry axis of the HP, this leg has to be in the contacts side of the HP (*i.e.* opposite side of the tip). Then, with a delicate procedure, the sample is aligned parallel to the HP by tightening or loosening the spring loaded screws in the back of the sample puck. Once the sample is perfectly parallel, we create the slight tilt by loosening (one and a half turn) the screw that was aligned in opposite side of the tip. At this stage, the sample is ready to be measured, the microscope can be closed and mounted on the fridge.

2.3 SHPM developement

In this section we describe the modifications we made to our microscope to improve the low temperature performance. The main issue we focused was to ensure a proper thermal contact between the sample and the MC. As measurements take place in the IVC, the SHPM head is under a high vacuum. The microscope was designed to work with exchange gas like in a variable temperature insert, the heat produced by the microscope and the heat from the sample was supposed to be removed via the exchange gas. In our case, the microscope itself is the thermal conductor. At the temperatures we are working at, most materials have a very poor thermal conductivity, there are very few phonons to carry the heat, it is conducted through conduction electrons. The microscope is mostly made of brass which has a relatively

poor thermal conductivity. Moreover, the heat from the sample has to go through the quartz tube, which is an insulator, so has an even lower thermal conductivity at dilution temperatures [17]. This will cause two principal problems. First, the sample will take long time to get the desired temperature. Second, if there is any heat load into the microscope, a constant temperature gradient between the sample and the MC will easily build up.

We use copper to improve the thermal conductivity from the sample to the MC. Copper has a thermal conductivity of two orders of magnitude higher than brass [17]. By using small amounts of copper we can significantly enhance the thermal link between the sample and the MC. We first replace the bottom of the sample puck by an identical piece, but made of oxygen-free high thermal conductivity (OFHC) copper, we gold coat it to preserve its surface from erosion and oxidation. We also drill 6 new holes to clamp down three copper braids, one coming from the sample holder, the other one coming from the bottom of the sample puck, and the main one going up to the main arm of the microscope. The OFHC copper piece will ensure all three copper braids are well thermalized to each other.. In figure 2.1 one can easily see the last copper braid. As we also use it to carry the tunneling current, we had to insulate it from the rest of the microscope, it was attached on the arm of the microscope with thin cigarette paper soaked with *GE varnish*.

For the long sample, we designed a small cylindrical OFHC copper piece to fit the sample in. The sample is 5 millimeters high and the copper piece is 4 millimeters (Figure 2.6). We first want to improve the thermal contact of the sample by attaching it directly to the copper string. Then it also improve its mechanical stability, it is very useful when polishing the top of a needle shaped sample. In the following figure one can see a picture of the sample puck with the mentioned modifications and the elongated sample mounted in it.

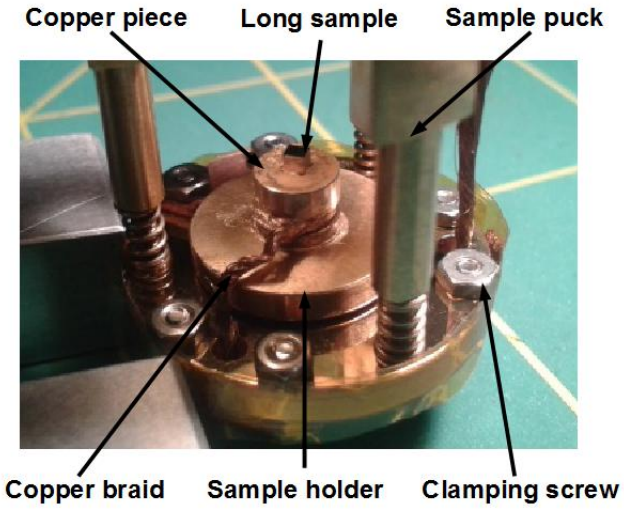

Figure 2.6: Picture of the modifications effectuated on the sample puck. The long sample is mounted on the sample holder inside its copper piece.

This system with 6 new small screws and a long string makes the sample preparation

slightly longer, but we have observed that it is very easy to build up a temperature gradient between the sample and the MC. To have better control of the temperature on the sample we attached a RuO_2 thermometer on top of the microscope itself, next to the neck of the microscope where the copper braid coming from the sample puck is wound (see Figure 2.1). Ideally, we would like to have a thermometer on the sample holder, but in practice there is not enough space, even for small thermometers. In the following figure (Figure 2.7) one can see a plot of the temperature measured by the MC thermometer and the RuO_2 thermometer during a normal imaging procedure. The system was left at base temperature for more than 60 minutes. Between the first two dot-dashed lines, the microscope was in the auto-approach mode, a pulse was sent into the slider piezoelectric every two seconds. Then, after allowing the sample to cool back down, two scans where performed (from min 40 to 60). Finally,between the last two dot-dashed lines, the sample was taken several steps away from the microscope by rapidly pulsing the slider piezoelectric.

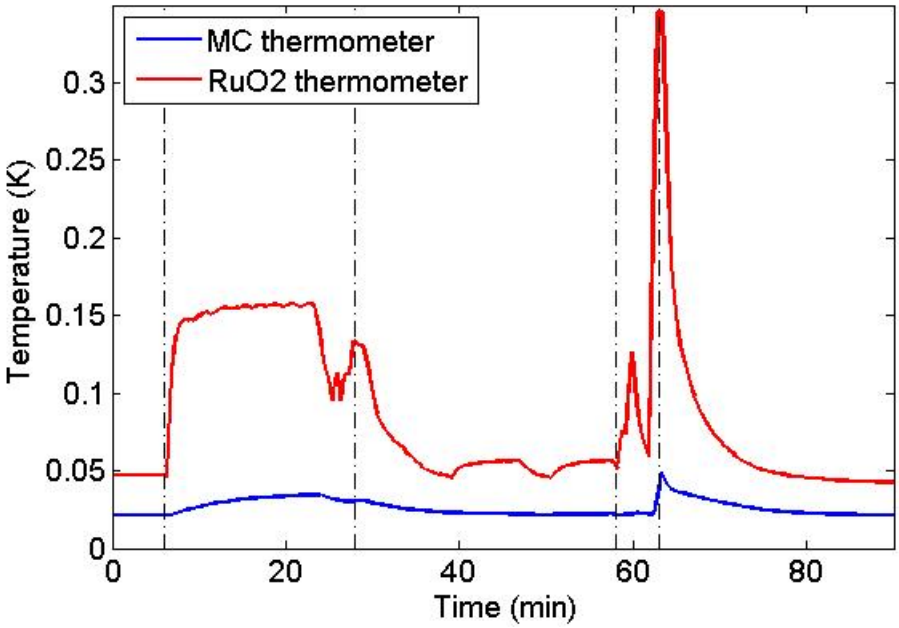

Figure 2.7: Measured temperature on the MC and the microscope neck *versus* time during an imaging procedure.

The first observation is that at base temperature both thermometers don't indicate the same temperature. One would expect that after a large enough relaxation time, both temperatures are the same. It is known that RuO_2 thermometers become unreliable at $T < 20 - 50$ mK. We attribute that divergence to an artifact of the thermometers. The error of the calibration of this RuO_2 thermometer diverges below 60 mK. For higher temperatures, the accuracy of the RuO_2 thermometer is guaranteed. One can then see that when approaching the surface the temperature on the microscope increases considerably while the temperature on the MC remains relatively constant. Heat dissipated into the microscope by the strong electrical pulse injected in the slider piezoelectric, and the mechanical friction between the sample puck and the quartz tube. The fact that it gets to a stable temperature during this process, tells us that

the amount of heat dissipated by the SHPM head compensates the heat pumped by the MC. The difference in temperature is not dramatic, but we have to take in account that the sample could be even warmer. When we retract the sample, the temperature on the microscope neck increases rapidly and reaches higher temperatures. In this case, the pulses are performed at a much higher rate. The power dissipated is higher but during a shorter time. Given this huge gradient, the actual temperature on the sample could be much higher. Fortunately, as one can see, between the minutes 40 and 60, when two images are taken (about 8 minutes each), the actual imaging process doesn't heat significantly the microscope head.

The information that we can extract from this graph is that one can actually take an image of a sample at very low temperatures by leaving the system relax to base temperature long enough. It also tells us that when some heat is dissipated in the microscope, it is very easy to create a thermal gradient between the head and the MC. We conclude that the efforts taken in improving the thermal conductivity from the sample to the MC where worthwhile. Ideally, we would like to replace all the brass of the microscope with OFHC copper. A further improvement could be implemented by thermally coupling the sample puck directly to the MC.

At temperatures around 1 K, we observed that there is almost no gradient of temperature between the MC and the microscope, regardless of the heat dissipated. From 0.1 K to 1 K, the thermal conductivity of brass increases by a factor of 10, and the thermal conductivity of quartz is three orders of magnitude higher [17]. The heat can therefore, easily be dissipated through the microscope.

Chapter 3

Qualitative observations of the magnetic domains

3.1 Ground state domain structure

As seen in the introduction, the rare earth compound $LiHoF_4$, is a dipolar-coupled Ising ferromagnet. One of the main motivations of this project was to observe its ground state domain structure. In their paper, Biltmo and Henelius, conclude that $LiHoF_4$ is an excellent playground for theories of domains because domain walls have no width, and domains appear naturally in *monte carlo* simulations [7]. They also propose a ground state configuration of the magnetic structure consisting of parallel sheets, and calculate an approximate width of the domains, for cylinders of different heights. For our experiments it is very difficult to obtain cylindrical shape crystals. In their calculations they don't take in account any edge effect, the only shape dependent variable is the demagnetization factor. The total magnetic field inside a magnet is the sum of the demagnetizing fields of the magnets and the magnetic field due to any free currents or displacement currents. The total field H inside an ellipsoidal magnet is $H_k = (H_0)_k - Nk(M_0)_k$. Where k are the principal axes in x, y and z directions, H_0 is the applied magnetic field, M_0 is the magnetization of the sample, and N is the demagnetization factor. By taking any shape that has the same demagnetization factor as a cylinder, we should obtain similar conditions to the ones they used to calculate the domain sizes. In our experiment it was easier to cut the crystals as rectangular prisms (*i.e.* regular cuboid). From calculated values in the bibliography, we get similar demagnetization factors for cylinders and rectangular prisms of similar surface to height ratios [18] [19]. More precisely we get 0.65, 0.33, and 0.10 as demagnetization factors along z for the flat sample, cubic sample, and long sample respectively. It also has been proved that the total demagnetizing field, and its gradient, are approximately the same for a semi-infinite prism and a semi-infinite cylinder [20].

We start by investigating images of the a-a plane taken at base temperature (below 50 mK) for the three different sample geometries. All images where taken using the maximum possible XY range at this temperature ($12 \times 12\ \mu m$). The images are 256×256 matrices of the hall signal converted into Gauss, by an built-in function of the software. One has to insert the standard "Ohms to Gauss" factor measured by *Nanomagnetics*, at 77 K for each HP. Given our observations, this factor might be wrong for sub-Kelvin temperatures, we found a factor two discrepancy for one of the Hall probes. The software not only normalizes the data, but

it also outputs the magnetization in a scale going from zero to its the maximum value for images taken with a positive hall current, and in a scale going from the minimum negative value to zero for images taken with a negative hall current. By rescaling the data to have zero as minimum magnetization we get the same images with positive and negative hall currents.

The first SHPM image we took at base temperature (21 mK) on $LiHoF_4$ is presented in figure 3.1. The image was taken on the flat sample with the STM tracking mode (or contact mode), as described in the introduction[1]. We observe a coarse domain structure that can be assimilated to a square lattice of discs. The discs diameter is around 4 μm, the lattice parameter is of about 8 μm. As we cannot get bigger images it is difficult to ensure this statement. Unfortunately, the system that should allow us to move the sample by pulsing the XY piezos, doesn't seems to work. There is also an underlying texture with smaller domains. In the following chapter we will discuss more precisely about the estimation of the size of this small domains, as we will see, the SHPM overestimate it.

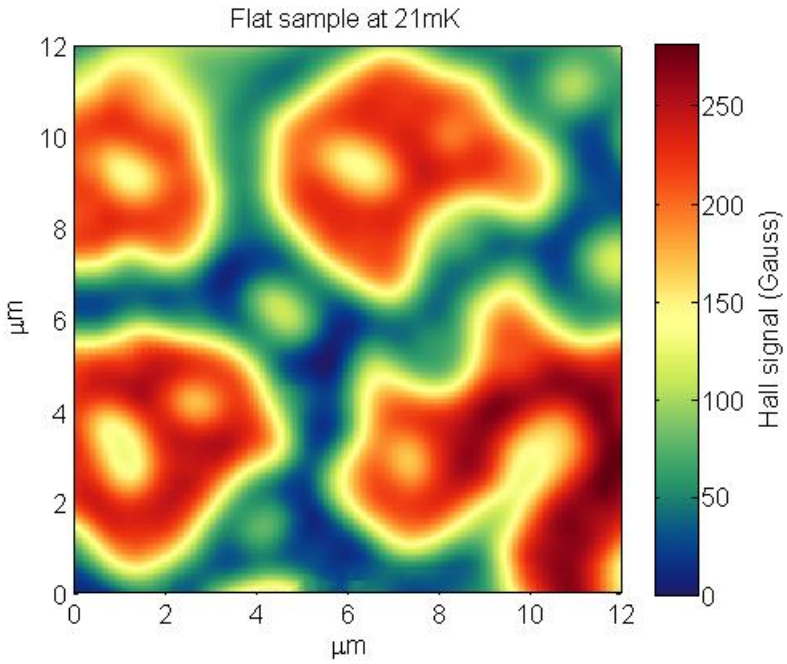

Figure 3.1: SHPM image on the a-a plane of the flat sample at 21 mK, taken with the contact mode.

The SHPM image of the cubic sample at 30 mK is presented in figure 3.2. This image was taken in the lift-mode, a distance of 200 nm was taken from the top of the sample. The first observation is that we get very similar domains as with the flat sample. The magnetization values are also very similar. The top right part of the image is the most reliable. Due to experimental problems (gold coating, sample mounting, etc.), there are many artifacts in the extreme left, and in all the bottom of the image. Nevertheless we see the same circular

[1]The STM feedback keeps the HP at a constant distance from the surface when scanning along X and Y.

shaped domains with a smaller underlying texture. We also see that there is not a strong enhancement of the image quality in the contact-mode compared to the lift-mode. Finally, the elongated sample was also imaged (Figure 3.3) with the lift-mode (200 nm lift distance) at 100 mK. It is obvious that the features increased size, but it seems that in a broad sense, the structure is the same (disc lattice).

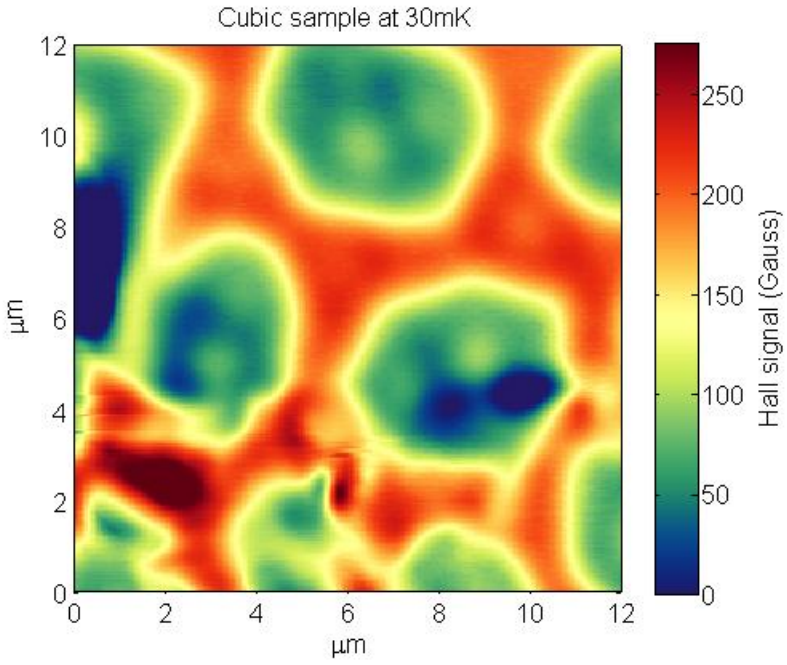

Figure 3.2: SHPM image on the a-a plane of the cubic sample at 30 mK taken using lift-mode.

One could argue that as we take this images at a finite temperature, we didn't reach the ground state. In the following section we will have a more detailed discussion about the evolution of the domains with temperature. At the base temperature of the fridge these structures are frozen, there is not enough thermal energy to move the domain walls. A strong experimental argument is, when retracting several slider steps from the surface and coming back again, we get the exact same image, even if as seen in the previous chapter (Figure 2.7), the temperature on the sample can get temperatures of few hundreds of milliKelvin. For the last sample (long), we warmed up the system up to the critical temperature, and went back to base temperature. In the following figure (Figure 3.4) we present the image obtained for this second cool-down.

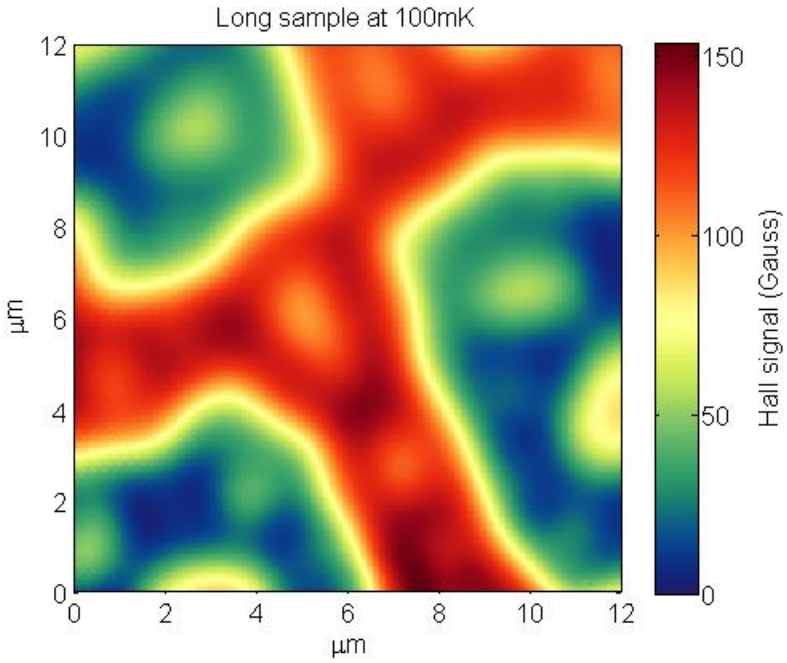

Figure 3.3: SHPM image on the a-a plane of the long sample at 100 mK taken using lift-mode.

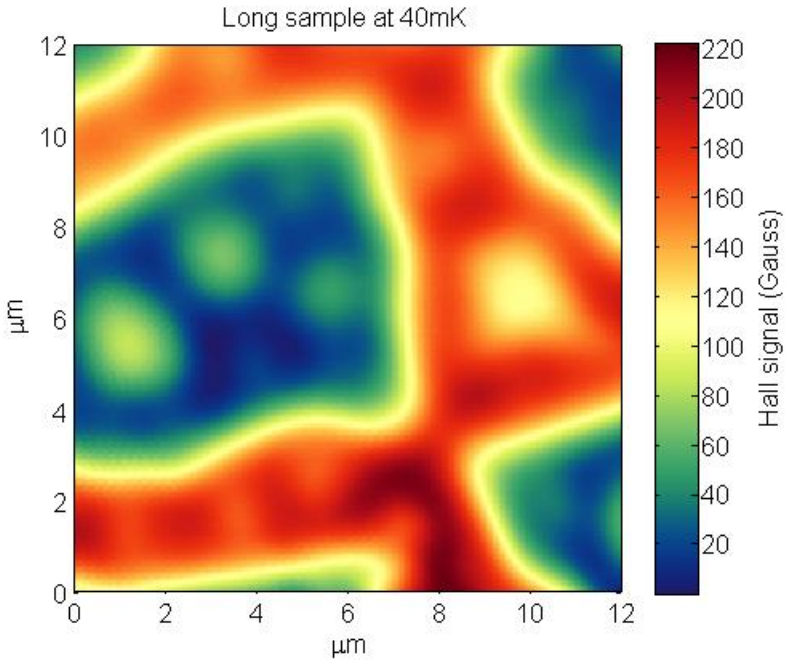

Figure 3.4: SHPM image on the a-a plane of the long sample at 40 mK taken using lift-mode.

We observe that the domain structure is very reproducible. The features seem to have similar size and shape. There is however a significant change in the amplitude of the Hall

signal. Even if we expect a decreasing of the magnetization strength with an increasing of the temperature due to fluctuations, we wouldn't expect such a significant difference for small temperature differences. Throughout this thesis, the Hall signal amplitude is not quantitatively analyzed except in a few specific cases where we paid special attention to it. For the three samples we had to use three different Hall probes, as two where damaged during the experiment. Also, between the last two images (Figure 3.3 and Figure 3.4), a very high current was accidentally driven trough the Hall probe, changing slightly its properties. Moreover, we didn't enter the proper "Ohms to Gauss" factor for all measurements. Nevertheless, we get very good information about the domain structure near the surface.

As expected, given the strong anisotropy of $LiHoF_4$ along the c-axis, and the AC-susceptibility measurements [21], the magnetic domains should be needle shaped along the c-axis. In figure 3.5 we show an SHPM image at the a-c plane of the cubic sample at 25 mK. When mounting the sample it was very difficult to accurately align the crystallographic axes with the scanning axes. Given we see parallel stripes, it is obvious that we indeed have magnetic domains aligned along the c-axis. There seems to be a slight enhancement of the strength of the domains as one goes to the bottom of the image, this is just an artifact due to the tilt of the sample. The bottom of the image is the closest point to the HP, for a tilt of 1.2^o over a distance of 12 μm, there is a difference in height of 250 which is enough to have a slight difference in the magnetic field intensity.

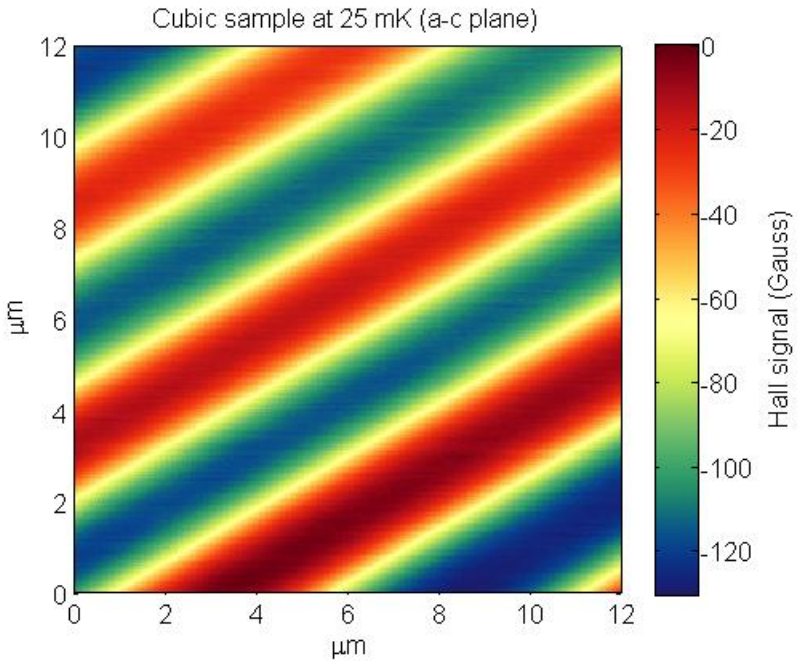

Figure 3.5: SHPM image on the a-c plane of the cubic sample at 25 mK (lift-mode).

It is striking how the thickness of these domains (3 μm) coincide with the diameter of the discs observed in the c-axis plane (also about 3 μm). We don't see any trace of stripe-like underlying structure, the magnetization looks very homogeneous within a domain. It could be that the underlying texture we see on the a-c plane, is due to spikes of opposite magnetization that form near the surface, the branching effect [8, 9]. In their paper, Meyer

et.al. perform magnetooptic microscopy on $LiHoF_4$ using the transparency of the crystal to focus their microscope directly into the sample at controllable depths (Figure 3.6) [11]. Their images look significantly different, despite focusing issues, it is because they have been taken under a longitudinal field of 0.7 T and at a temperature of 1.3 K. Nevertheless, they also observe cylindrical domain structure with small spike-like domains near the surfaces. In our chase we have a much higher resolution, but we are not able to ensure that there is a branching effect near the surface, as we just image the side of the magnet.

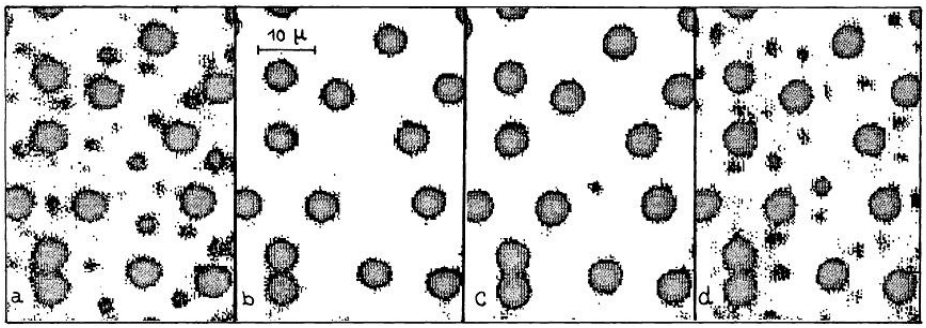

Figure 3.6: Magnetooptic microscopy on $LiHoF_4$ under a longitudinal field (7 T), focused on the top surface (a), at half of the sample thickness (b), at 3/4 of the thickness (c), and at the bottom surface. (Taken from [11])

Taken together, all these observations indicate that the domain structure of the ground state is a lattice of needle-like domains. In their discussion about the domains configuration, Biltmo and Henelius use minimization of the energy to prioritize parallel sheets configuration instead of needle-like cylinders [7]. We also see that, inside a domain, there are smaller domains of opposite magnetization that have a strong effect on the shape of the bigger domains. It could be that the branched states make the cylindrical domain configuration more efficient. For a small demagnetization factor (long sample) we obtain relatively large domains ($\sim$ 9 μm), whereas for the cubic and flat sample we obtain smaller domains ($\sim$ 3-4 μm). It would be worth undertaking further measurements, with well defined sample geometries, to find a more precise correlation between sample shape and domain size.

3.2 Domain dynamics with temperature and transverse magnetic field

In this section we present SHPM images taken under different temperature and magnetic field conditions. We will first show the changes of both a-a plane and a-c plane images with increasing temperature. In the second part we present the effect of a transverse magnetic field (*i.e.* perpendicular to the c-axis). Due to the geometry of our experiment, we have only images of the a-c plane under transverse magnetic field. Then, we will discuss the freezing of the domains at low temperature. Finally, we will show an image preformed while the sample was undergoing a phase transition.

3.2.1 Increasing temperature

We present successive SHPM images taken on the a-a plane of the elongated sample (Figure 3.7), as we where warming the DR from base temperature to the critical temperature. This is not a trivial operation, as the fridge is supposed to be used in a range of temperatures from base temperature to 800 mK. One can also measure from 0.8 K to about 10 K by circulating only 10 percent of the mixture. The problem is that the fridge has to be warmed up to 4 K to switch between these two modes, so the specific domain structure would be lost. For this set of temperatures we managed to warm it slowly in a controlled way, but it is not the case for all measurements.

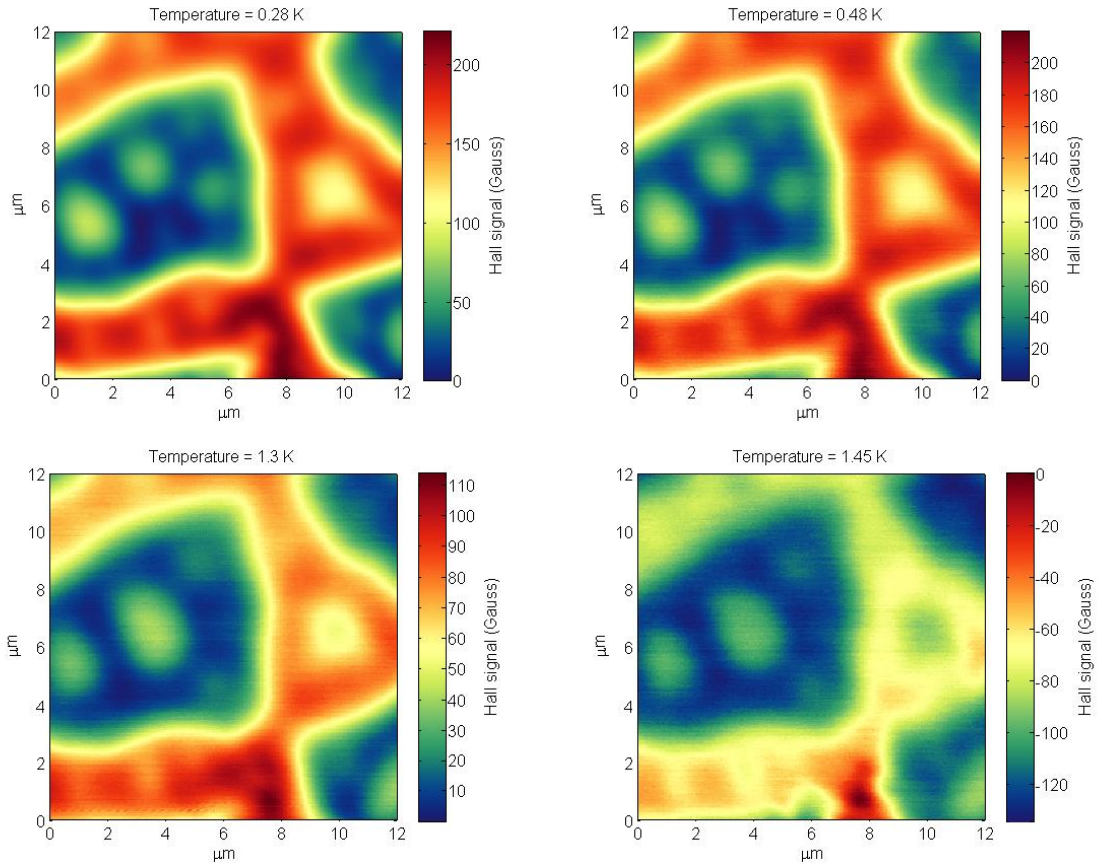

Figure 3.7: SHPM images on the a-a plane of the long sample at different temperatures taken using lift-mode.

We can see that the domain shape on the a-a plane surface doesn't change from the ground state (Figure 3.4) to 1.45 K, almost the critical temperature. One can also say that the values of the Hall signal Between the up and down domains decreases. To better understand these observations, we present in figure 3.8, the difference of absolute value of the Hall signal of the image obtained at base temperature and the one obtained at 1.45 K. It is immediately clear that the domain boundaries don't move, and that the Hall intensity within a domain increases at low T. This observation is consistent with the increase of the expected value

of the magnetization as we decrease the temperature. We also notice that the underlying texture doesn't seem to change much. In the following chapter we will use the complete set of measurements to extract a meaningful measure of the magnetization *versus* temperature.

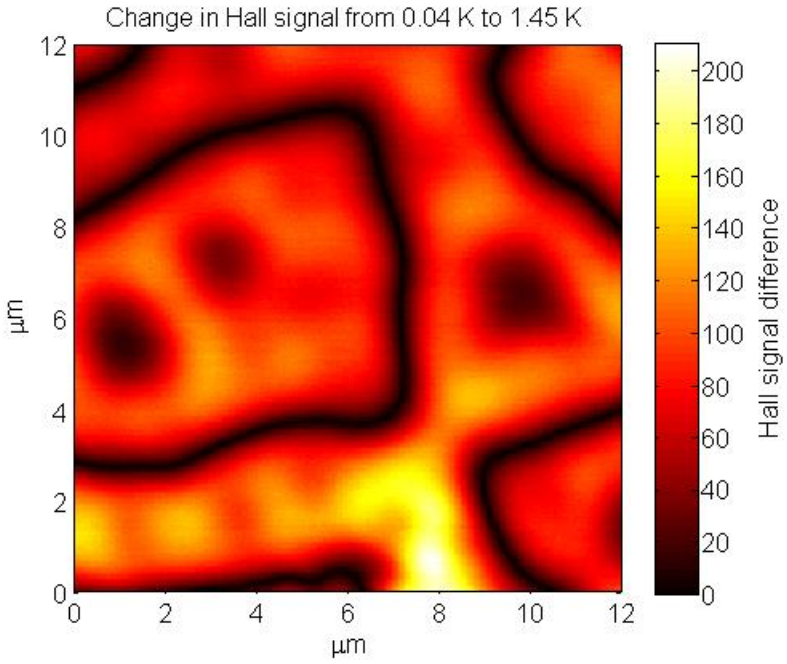

Figure 3.8: Absolute value of the difference of the SHPM images taken on the elongated sample at 40 mK and 1.45 K.

For the cubic sample we also imaged the a-c plane at different temperatures (Figure 3.9). As a first observation, the image obtained at 850 mK, is different from the image at 25 mK (Figure 3.5). These images belong to a different set of measurements performed from 800 mK to 1.6 K, for this set of measurements, we warmed up the fridge up to 4 K and then condensed 10 percent of the mixture to have a better control of the temperature. We assume from the previous observations, and from the fact that it doesn't change in a wide range of temperatures, that the domain structure we observe on the a-c plane at 850 mK, is the ground state. Its domain width is slightly larger than the one observed in figure 3.5, probably due to the remanent field in the electromagnet. All SHPM measurements of the ground state on the a-c plane performed after the transverse field study (see next chapter) present slightly wider domains. As the magnet went up to 3 Tesla, we have a small remanent field orientated transversally to the c-axis, we will see in the next chapter that even a small field have a significant effect in the domain size. In the image at 1.2 K we have essentially the same domain structure. At 1.4 K we have an additional high signal (red) domain, and therefore all the domains are thinner. At 1.5 K there are even more domains and their thickness is smaller. The overall signal contrast between up and down domains also decreases significantly.

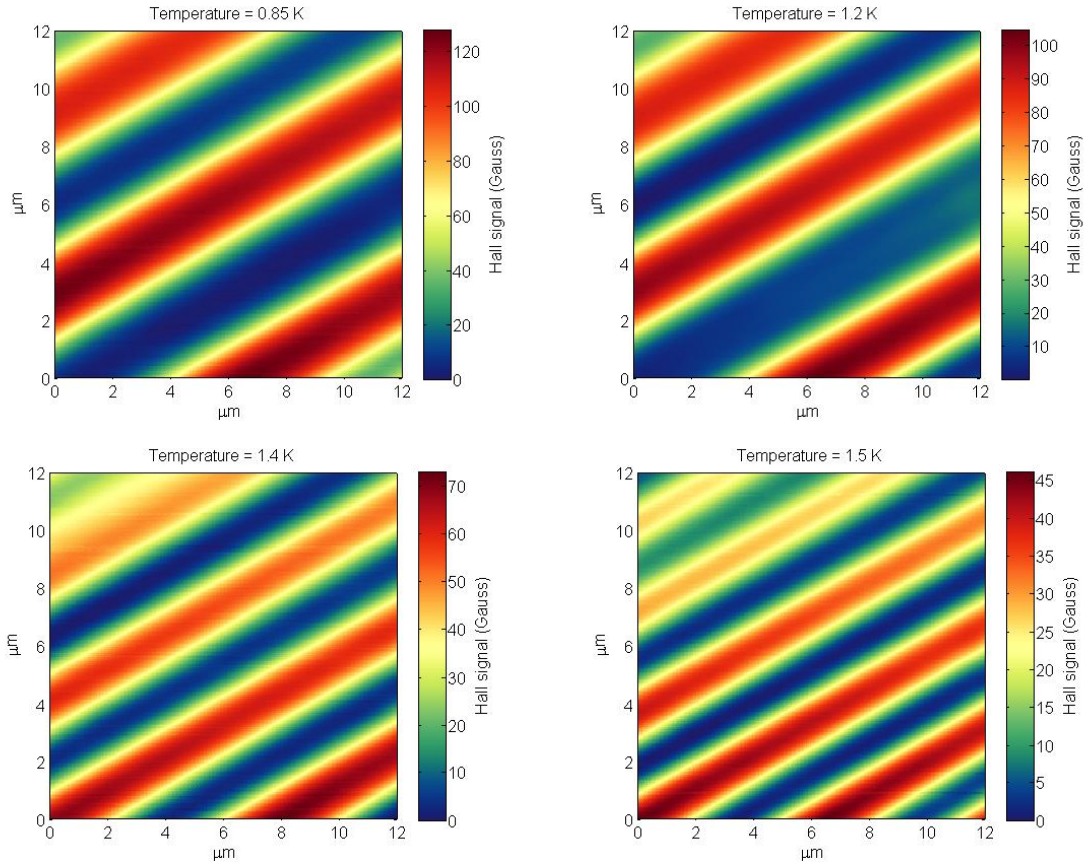

Figure 3.9: SHPM images on the a-c plane of the cubic sample at different temperatures using the lift-mode.

Upon first inspection, it seems that the observations on the a-a plane and the a-c plane only agree in the decreasing of the intensity of the domains as the temperature increases. This is easily explained by the fact that the mean magnetization inside a domain decreases as the temperature increases. To explain how, in the a-a plane we observe that the domains don't move up to the critical temperature, whereas in the a-axis plane we observe a significant change in the domain width at lower temperatures, we use again the branching mechanism. In the image taken at 1.2 K on the a-c plane (Figure 3.9), there seems to be a spike of opposite sign magnetization entering from the right into the wider low signal (blue) domain. It seems likely that it is the prelude of the "red" domain that appears at 1.4 K. It has been suggested by Gabay and Garel [9] that increasing the temperature in a dipolar Ising magnet favors branching. If, as we suggested the underlying texture observed in the a-a plane at the ground state corresponds to branched spikes under the surface. The observation would be consistent with the fact that at high temperatures, the spikes become longer and longer and get to cross the whole crystal, creating a more dense domain structure, like that seen in the a-c plane images.

3.2.2 Increasing transverse magnetic field

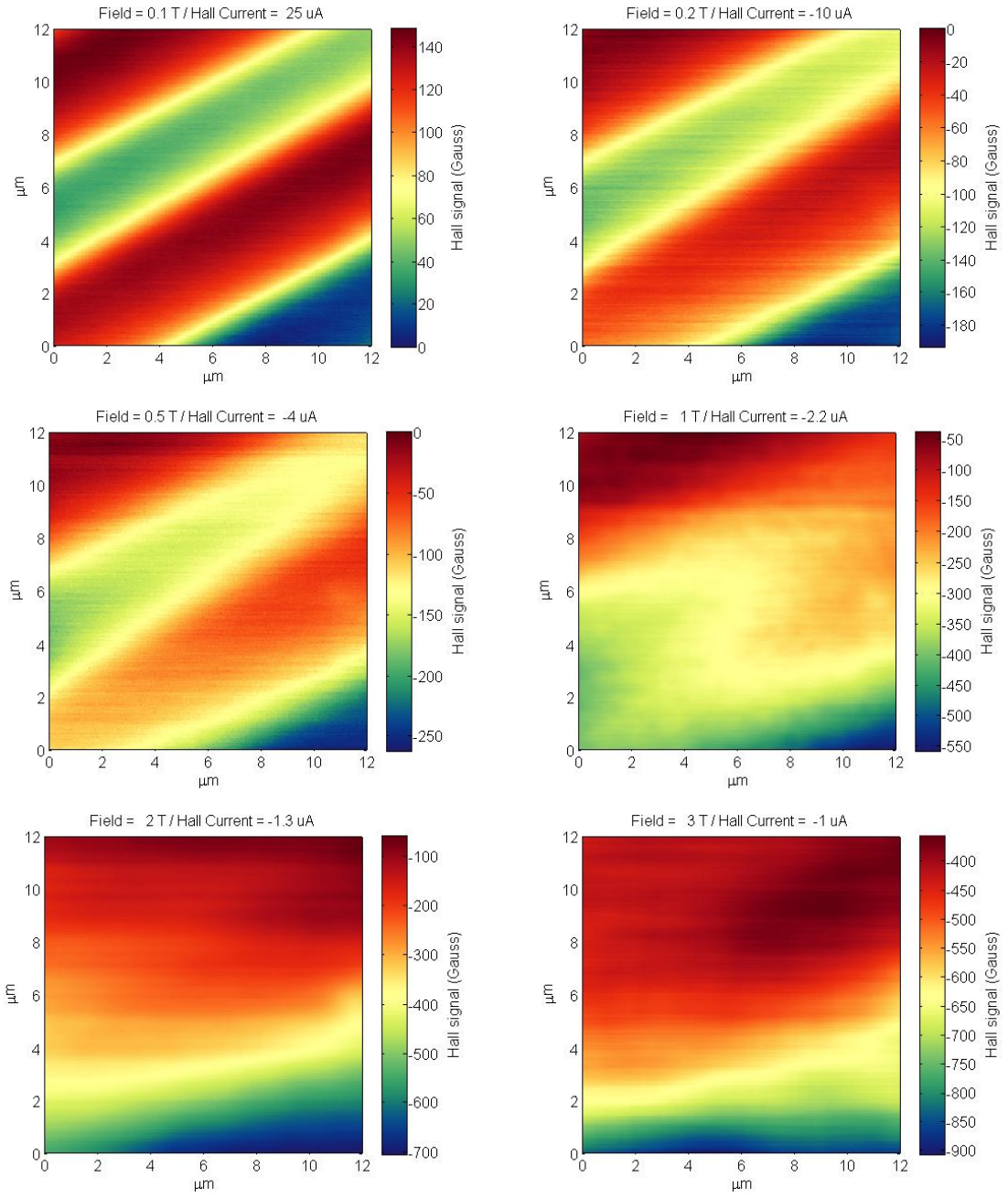

Figure 3.10: SHPM images of the a-c plane of the cubic sample under different magnetic field taken with the lift-mode. The images for the 3 highest magnetic fields were smoothed to minimize noise. All images were taken below 30 mK.

As described by Bitko *et. al.*, $LiHoF_4$ presents a quantum phase transition driven by a transverse magnetic field at T = 0 [4]. We are interested in having direct observation of the magnetic domains when approaching this transition. In figure 3.10 we present six SHPM

images on the the a-c plane of the cubic sample with magnetic fields 0.1, 0.2, 0.5, 1, 2, and 3 Tesla. All images were taken at temperatures between 20 and 30 millikelvin. Ideally, we would like to apply transverse fields close to the critical field ($\sim$ 5 T). In practice, we face two principal problems that make higher field images meaningless. First, the domains size becomes too large for the field of view of the microscope, and second, the noise level of the images starts to get very significant compared to the signal. The first problem would require modifying the design of the microscope. The second problem is related to the fact that one has to lower the Hall current as the field increases to avoid saturating the signal, and therefore the electrical noise increases. As a partial solution to reduce the noise, we applied an averaging filter on the three images at higher fields. It would be more interesting to modify the preamplification stage of the Hall signal to be able to measure Hall voltages larger than 10 V (*i.e.* work with higher hall currents). Ideally, we would also like to image the a-a plane under these conditions to better understand the phenomenon, but as mentioned, our present setup doesn't allow us to apply a magnetic field perpendicular to the axis of the microscope.

In the image at 0.1 T (top left panel of figure 3.10) one can already see a big increase (from 3 to 7 microns) in the domain width compared to the zero field image (Figure 3.5). At 0.2 T the domain boundaries start to deviate from a parallel position, and the domains appear to have a wedge-like shape. It is even more obvious at 0.5 T, where the two middle domains seem to be shrinking from opposite directions. In the following images it seems that there is the creation of two big domains, and the domain boundary seems to be smeared within this process. Over all these images, the hall signal range seems to increase considerably. Another interesting observation is that from the first image, we can already anticipate the two dominant domains that will be created at higher fields, as the domain (green) that is sandwiched between the two higher signal domains (red) has less contrast with the opposite sign domains than the lower one (*i.e.* less intense).

It is striking to see how with a very small transverse field compared to the critical field, the domain structure changes significantly. As seen in the previous subsection, one has to increase the temperature much more significantly (compared with the critical temperature), to have such a change in the domain structure. Each of these two parameters implies a different physical mechanism. The temperature simply increases the thermal energy proportionally to K_BT, whereas the transverse field allows quantum tunneling from a spin orientation along the c-axis to the opposite spin orientation [4]. Apparently, with a small transverse field, the tunneling rate is high enough to allow the reconfiguration of the magnetic domains. In their study of the doped compound $LiHo_xY_{1-x}F_4$, Silevitch *et.al.* , observe that at low temperature ($T \ll T_C$), applying a transverse field results in a narrowing of the hysteresis loop due to the increase of domain wall tunneling [12]. They also propose that in the quantum tunneling regime ($T \ll T_C$ and $H_t \neq 0$), the Heisenberg uncertainty principle implies broadened domain walls. Due to the finite size of our probe ($\sim 1\mu m^2$), it is difficult to directly observe the domain wall thickness. In the next chapter we will attempt to determine it. As the field of view is small related to the size of the domains, it is impossible to extract in which amount the magnetic domains change their size and shape under high transverse magnetic field. From our observations it seems likely that there is an "unbranching" mechanism where some domains retract in a spike shape.

3.2.3 Freezing of domains

We present the sequence of measurements that was performed on the a-c plane of the cubic sample right after the field dependence study in the figure 3.11. The first image taken at 0.1 T (coming from 3 T), presents very large and diluted domains, compared to the one at the same transverse field (coming from 0 T) in figure 3.10. The successive image, taken at 0 T (coming from 0.1 T), shows also much bigger domains than what was expected for the zero-field-cooled ground state. Heating the sample up to 0.6 K at zero field results in the magnetic domains becoming substantially smaller. Once we get back to base temperature (still at 0 T), the domain structure remains the same as it was at 0.6 K. As we discussed in the beginning of this section, due to the remanent magnetization in the electromagnet, the domain width of the ground state is expected to be slightly larger than in figure 3.5.

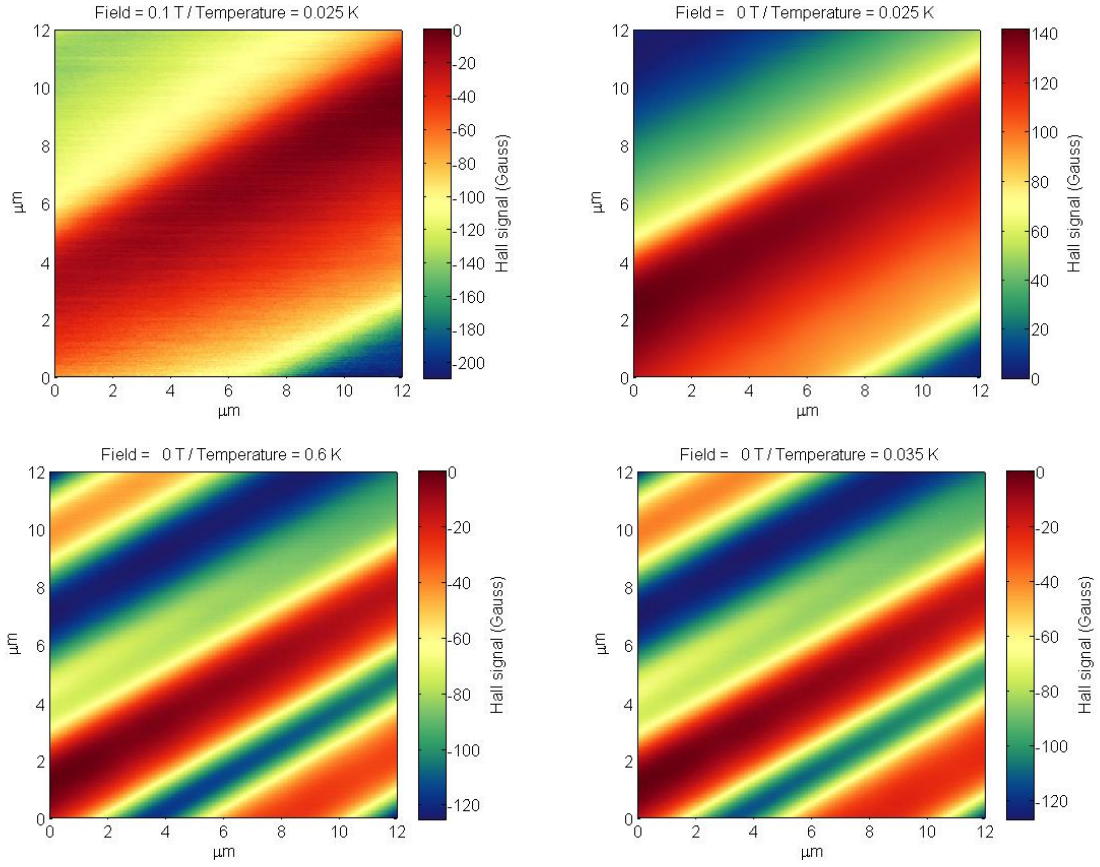

Figure 3.11: SHPM images on the a-c plane of the cubic sample after being at High transverse magnetic field (3 T). The images are chronologically ordered from left to right and top to bottom.

By comparing the two last images in figure 3.11 we can say that the ground state configuration in a thermal annealing, is determined at higher temperatures where the thermal fluctuations are strong enough to move the domain walls. We also observe that for the same positions in the phase diagram of $LiHoF_4$·($H_t = 0.1$ T / $T = 0.025$ K and $H_t = 0$ T / $T = 0.25$

K), we get different domain structures depending on which of the two control parameters was used to get there. Even if we didn't get to the paramagnetic phase in either of the two directions, we can compare this phenomenon to Quantum annealing. For the doped compound $LiHo_xY_{1-x}F_4$, it has been shown that the magnetic susceptibility at an identical place in the $H_t - T$ plane arrives at different value depending on the annealing protocol [13]. Pure $LiHoF_4$ doesn't present a spin-glass phase, but the dependence of the domain structure on the path over the phase diagram, suggest that at low temperatures ($T \ll T_C$), the domains are in a frozen state. They also suggest that for complex systems, and if barriers between adjacent minima are very high yet sufficiently narrow, quantum tunneling might be a more effective mean at energy minimization than a pure thermal process, with the potential to hasten convergence to the ground state. It would be legitimate to question which of the two process (thermal annealing or quantum annealing), leads to the minimum energy state.

3.2.4 Direct imaging of a phase transition

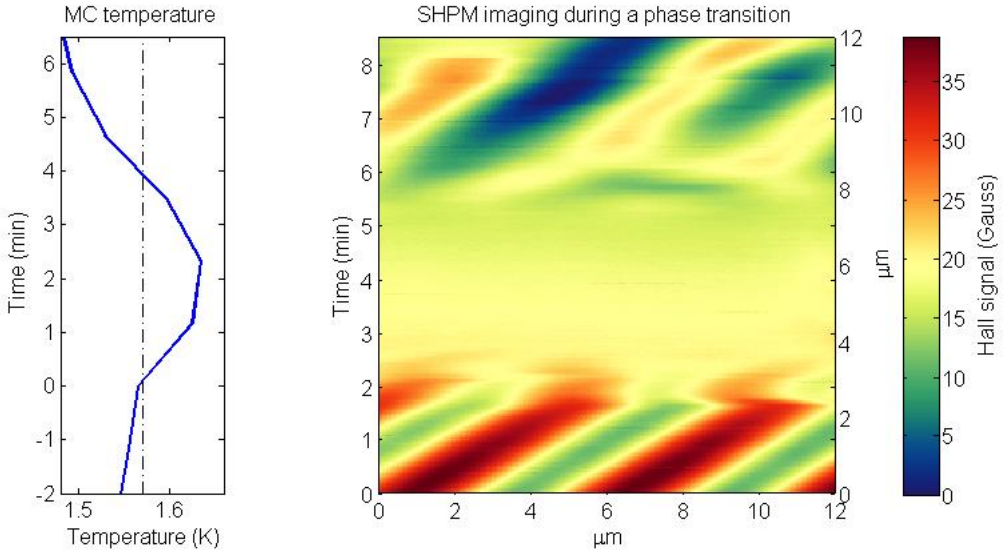

Figure 3.12: SHPM image of the a-c plane of the cubic sample (right) when the temperature on the mixing chamber was going through the critical temperature. An additional axis on the left of the image indicates at what time every line was recorded. Time synchronized with the image *versus* mixing chamber temperature (left). The dot-dashed line indicates the critical temperature.

During the temperature dependence study of the a-c plane magnetic structure, we managed to record an image during the time that the sample was undergoing a transition from the ferromagnetic phase to the paramagnetic phase, and a second transition back to the ferromagnetic state. In figure 3.12 we present this image (right) next to a graph where we show the recorded temperature in the mixing chamber at that time (left). We added an extra axis on the left of the SHPM image to give a temporal dimension. The 256×256 pixels image is taken line by line, from bottom to top. Every line takes about 2 seconds to be recorded, the full image takes about 8 minutes and 30 seconds, we can then assign a time to every line. On the left figure, the time is set to be zero at the start of the image acquisition. We

have set an offset of two minutes. As discussed in the previous chapter, the mixing chamber and the sample are not in thermal equilibrium. We assume there is a lag of two minutes within the temperature in the sample and in the mixing chamber. Finally, the dot-dashed line indicating the critical temperature in figure 3.12, is actually set at 1.57 K instead of the known critical temperature for $LiHoF_4$ of 1.53 K. This choice was made regarding the time spent over the phase transition in the SHPM image. It is possible of course that the thermal gradient within the mixing chamber and the sample accounts for that difference, but either way the discrepancy (0.04 K) is about 2.5%, which is smaller than the calibration accuracy of the thermometer.

This observation opens the possibility of studying this phase transition in a different way. If we would be able to have a better control of the mixing chamber temperature (for example optimizing PID parameters), and record the temperature directly on the sample, we could directly observe the domain dynamics critically close to the phase transition. The image acquisition time could be drastically decreased (to few seconds), losing spatial resolution, but opening the possibility to track the motion of the domains.

Chapter 4

Quantitative analysis

4.1 Intrinsic blurring

In this section we attempt to sharpen the SHPM image to get a precise measure of the domains size and its underlying texture. The main issue we have is related to the finite size of the Hall probe ($1\mu m^2$), and that we image at a certain distance of the surface ($\sim 1\mu m$). What we are presumably imaging are areas of opposite magnetization with very sharp walls (infinitely small at this scale), where within a domain, the magnetization is constant [7]. One first approximation would consist in dividing the hall signal scale into two parts, every pixel that is higher than a certain value belongs to an up domain, and every pixel that is lower belong to a down domain. In the figure 4.1 we present an SHPM image (left) and its corresponding magnetic structure (right) according to our first approximation.

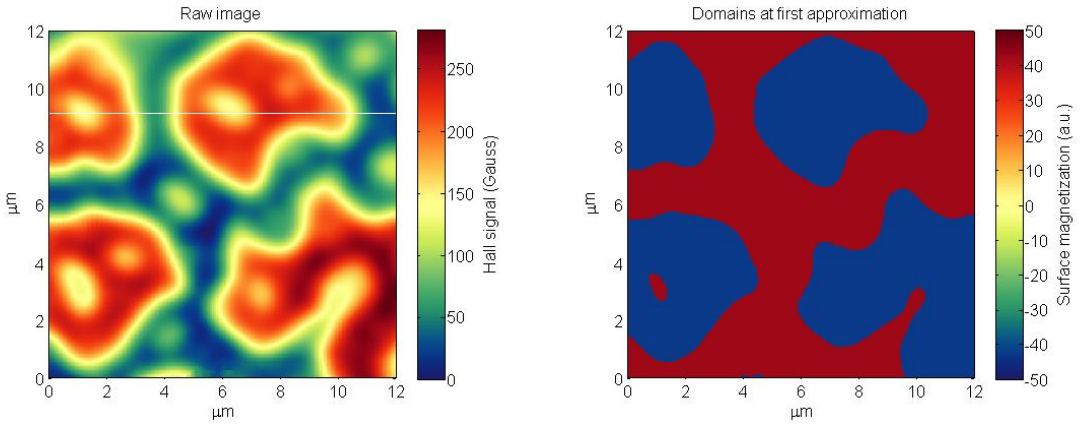

Figure 4.1: Raw SHPM image (left) with a white line indicating where the transverse cut is taken. Domain structure approximated by a simple method (right).

This approximation seems to represent the main structure well, but is almost totally blind to the underlying texture. A second approximation would consist of looking at the sign of the second derivative in x and y directions. This way we are able to separate the parts of the image with a different curvature sign (*i.e.* concave or convex). In the figure 4.2, we present the resulting magnetic structure (left) obtained with the derivative method. For this method

one has to filter the raw data to smooth it, therefore we lose information on the edges of the image. The frame is reduced by 1 micron from every edge.

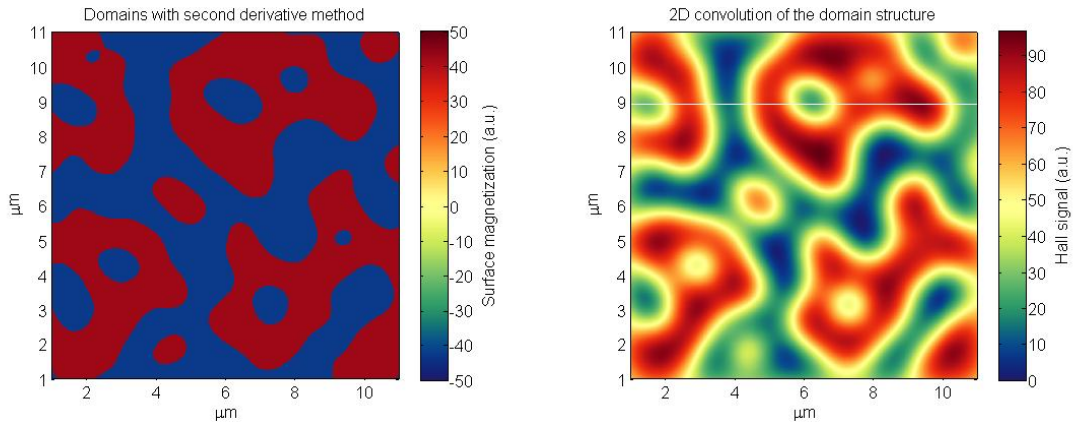

Figure 4.2: Domain structure approximated by the second derivative method (left). Two dimensional convolution of a Gaussian profile with the domain structure obtained with the derivative method (right).

The magnetic field at a certain point over the surface will be the sum of the contributions of all the magnetic domains near that point. Moreover, due to the size of the hall probe, the hall signal is an integration of the magnetic field over a squared micron surface. As an example of what the SHPM image of the domain structure obtained by the derivative method would look like, we perform a two dimensional convolution of the domain structure with a Gaussian matrix. Regarding the considerations above mentioned we use a 2 micron sized Gaussian with a standard deviation of 1 micron. The resulting image is presented in figure 4.2 (right). At first sight, it is quite similar to the raw image. In a more critical examination, it is obvious that the contrast between the underlying texture and the main domains is much higher in the reconstruction. To have a better understanding of the problem, in figure 4.3, we plot a horizontal cut of the SHPM raw image over the white line represented in figure 4.1 (left). In the right side of the figure, we plot the corresponding horizontal cut of the reconstructed image using two dimensional convolution. The dot-dashed line represents the Hall signal value we use to separate up domains from down domains.

The two profiles in figure 4.3 are considerably different. Despite the absolute unit discrepancy which is irrelevant, as the units in the reconstruction are arbitrary, the main difference is in the depth of the two "down" domains centered around 1 and 6 microns. With the second derivative method we overestimate the underlying texture features. Assuming that the magnetization within a domain should be constant, the only explanation is that we overestimate the size. To have a transverse cut as in the raw image, the features centred at 1 and 6 microns should be smaller "down" domains.

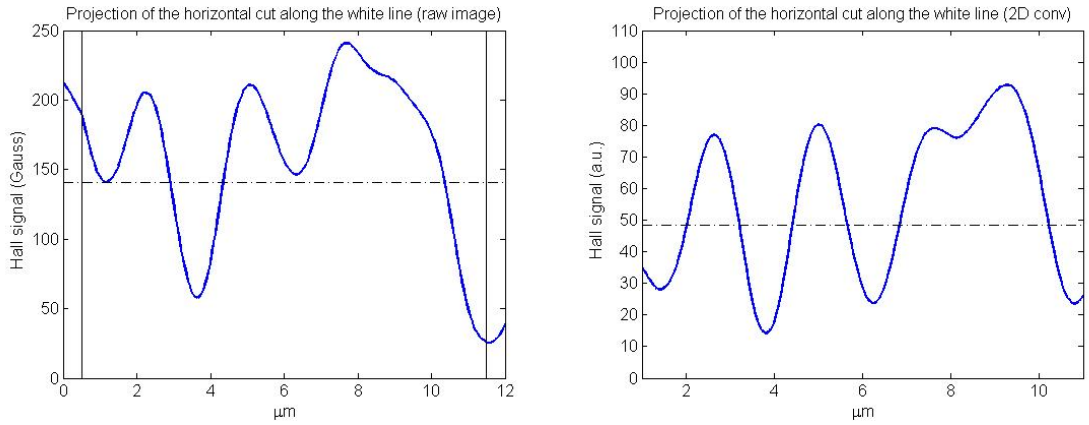

Figure 4.3: Horizontal cut of the hall signal over the white line in the SHPM raw image (Figure 4.1) (left). Horizontal cut of the reconstructed image in figure 4.2 across the white line (right).

From the former observations, we can state that a domain which has a small size relative to the hall probe, will be smeared out by the surrounding domains. In the following figure (Figure 4.4) we present a small simulation to better understand the imaging mechanism. We manually create a possible domain profile that matches quite accurately the horizontal cut along the SHPM image, after a one dimensional convolution with a Gaussian (2 micron sized and 1 micron of standard deviation). We extend the domain profile and the convolution in both directions to better match the measured profile. The SHPM image is also influenced by the domains immediately outside of the 12×12 microns frame.

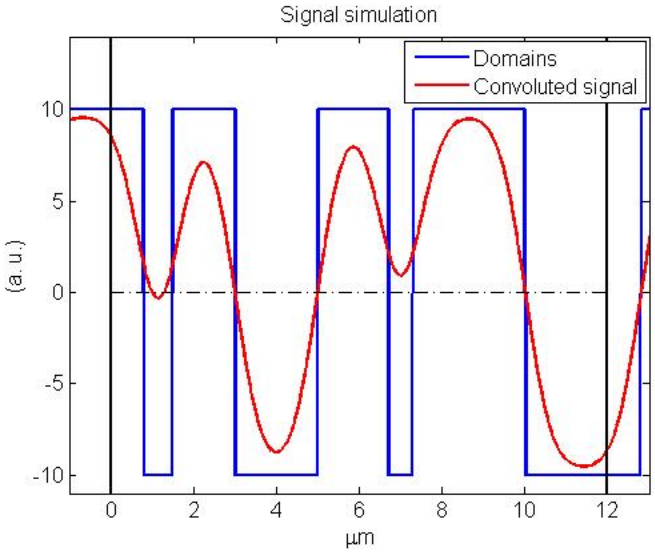

Figure 4.4: Simulation of a possible domain profile and its resultant SHPM signal.

We can see that the depth of the features in the SHPM image will not only depend on the domain magnetization, but also on the size of it. We also see that for domains whose

size is large compared to the hall probe size, the domain wall position coincides with the middle of the signal scale. It is why the first approximation of image treatment used in this chapter works for the main domain structure. As we suggested in the previous chapter, it seems that within each domain (disc or background), there are much smaller areas of opposite magnetization.

To have a complete reconstruction of the magnetic structure we would need to perform a two dimensional deconvolution. It happens to be a very complicated mathematical problem, that becomes even more complicated whenever adding experimental noise to the image. The one dimensional deconvolution of the cross sections of the figure 4.3, using a standard deconvolution algorithm fails. Even a standard deconvolution, of the convoluted signal in figure 4.4 is not stable over the whole range, it gives exactly the the original domain structure over the first 6 microns, but then it diverges to plus and minus infinite. Implementing an algorithm similar to the deconvolution but that takes in account the correct picture (opposite domains of constant magnetization with infinitely small walls) should be able to give better results. Ideally we also would like to know the exact profile of the probe. Here we use a Gaussian profile, but what we really need is a point spread function (PSF), the image obtained from a point-like magnetic object. One way to obtain it would be to image a surface with nano-magnetic spots (much smaller than a micron) imprinted on it. A different approach, close to the used in the simulation, would consist in randomly create domain structures and compare their two dimensional convolution with the image. By a chi-square method we could select the most likely to match the real structure.

Finally we would like to make two comments about some open questions from the previous chapter. First, if we understand that the domain configuration correspond to cylindrical domains deformed by an underlying structure associated with the branching mechanism. One could expect to have more than one branch, *i.e.* an extra domain of opposite magnetization inside the first one. We studied this possibility with the same method as before, by enlarging the down domains centered at 1 one and 6 microns, and adding a small (0.1 micron) inner domain of opposite magnetization. We obtain a very similar profile as before, as the features are smeared out by the convolution, the slight enlargement of the down domain is almost perfectly compensated by the small inner domain of opposite magnetization. At this stage, is it impossible for us to state if this is the case in the inspected images. An appropriate image treatment as described in the previous paragraph, should be able to discriminate between these kind of features, at least to a small extent.

We also mentioned that in the a-c plane images under high transverse field (Figure 3.10), the wall thickness seemed to increase. We used the same kind of simulation as in figure 4.4 to investigate it (Figure 4.5). What we conclude is that in a simple domain transition, an apparent increase of the domain wall in a SHPM image should be related to an increasing of the domain wall. When looking at a more complicated configuration, with the main domain wall formed by successively thin domains of opposite magnetization (keeping the domain wall infinitely thin), the apparent wall domain in the SHPM image would be broader. Anyway, this conjecture exercise becomes even more complicated because the mechanism in which we see the a-c domains is not well understood. With pure horizontal magnetic moments, the magnetic field should be parallel to the surface at all points, and therefore the Hall signal very weak. Surprisingly, we get contrast from one domain to the other similar to what we

have on the a-a plane.

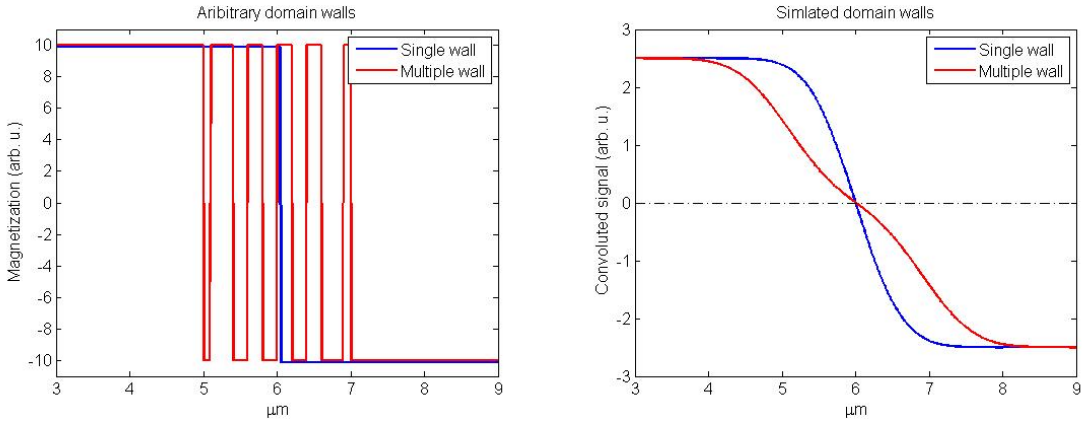

Figure 4.5: Simulation of two possible domain wall profiles (left). Convolution of the domain wall profiles with a Gaussian probe (right).

4.2 Magnetization

As we have seen in the previous chapter, when we increase the temperature, the signal contrast between the different domains decreases. We assume that it is due to, as expected, the decrease of the single ion magnetic moment (J) because of the increasing thermal fluctuations. Our goal here is to be able to quantify in a meaningful way this change in magnetic moment, and therefore magnetization. The problem is that, in the way the SHPM software treats the image, there is no zero reference for the magnetization. The only meaningful quantitative information is the difference in signal between two pixels, not its absolute value. A simple approach would then consist in comparing the signal between an up and down area, but as we have seen in the previous section, there is a strong shape and size dependence on the intensity of the signal. We decided to use a statistical approach to extract the change in the mean magnetization. In figure 4.6 we present a histogram of the number of pixels *versus* the Hall signal (right) for the SHPM image taken on the a-a plane of the long sample (left). The blue dots on the histogram represents a fit of two Lorentzians.

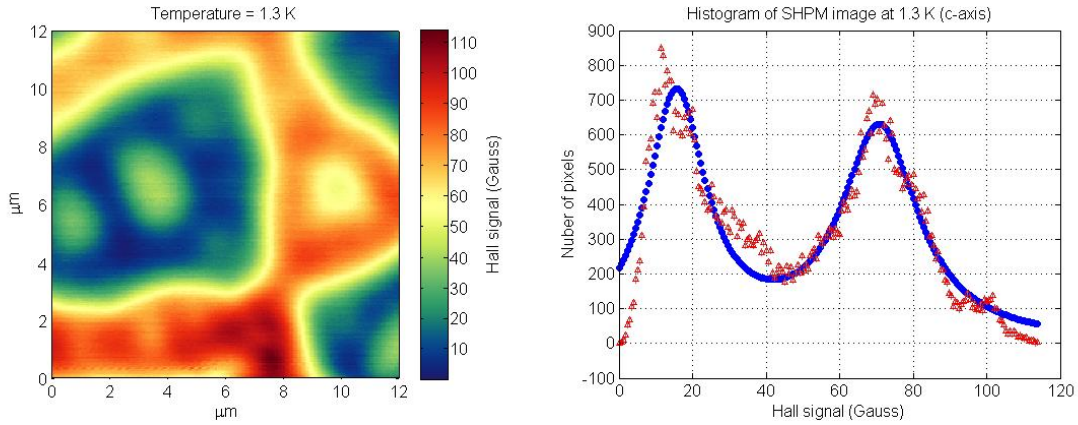

Figure 4.6: SHPM image on the c-axis plane of the long sample at 1.3 K (left). Histogram representing the number of pixels *versus* Hall signal of the SHPM image (right).

We observe that the histogram presents two clear peaks. By plotting the histogram, the shape and size effects over the up and down domains are averaged into the the two peaks. Even if there is a clear underestimation, we believe that the difference between the center of these peaks, is proportional to the mean magnetization. We fit different Lorentzians with the same half-width at half-maximum to each peak to find a good estimation of the center of each. One could use also a Gaussian, but as the peaks are relatively sharp, the Lorentzians give a better fit. We repeated this process to the full set of temperature dependent SHPM images on the a-a plane of the long sample to obtain a magnetization curve. The images from different cooldowns seem to not be directly comparable in this method. As we have an image with features of different sizes and shapes, the separation of the peaks will not be comparable. Therefore it is obvious that even if the Hall signal has a physical unit, the magnetization extracted in this way is in arbitrary units.

The magnetization curve extracted with the histograms method is shown in figure 4.7. As we expected the magnetization decreases with temperature, and goes to zero as we get closer to the critical temperature (1.53 K). After scaling the data, we compare it to neutron diffraction measurements performed by P. Babkevich and I. Kovacevic in our group (unpublished). This data was obtained by looking at the change in the intensity of the nuclear Bragg peak once we enter to the ferromagnetic phase. Both, the histogram method, and the neutron experiment, seem to coincide in the typical profile. For temperatures close to the phase transition, the magnetization follows: $M \propto (T_c - T)^{\beta}$, where the mean-field value of β is 1/2. The slight decrease of the magnetization as we get to zero temperature for the neutron data, might be related to the change of the scattering cross-section due to the nuclear moment.

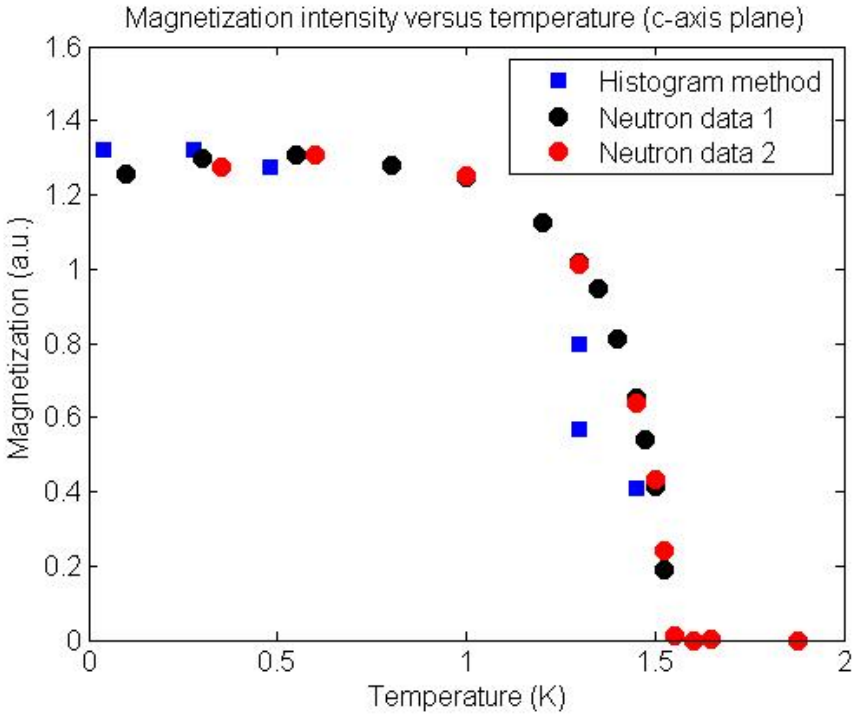

Figure 4.7: Magnetization *versus* temperature extracted from fitting the histograms obtained form the a-a plane SHPM images of the long sample, compared to experimental data obtained with neutron diffraction.

For the temperature dependence set of measurements on the a-c plane, we also performed the same type of study. In figure 4.8 we present the calculated magnetization *versus* temperature, and we also compare it with the data obtained from neutron diffraction. As we mentioned before, we don't fully understand why we see the a-c plane images the way they are, but it seems even more obvious with this study, that the intensity of the domains we see is related to the magnetization along the c-axis. As before, we seem to have a reasonable agreement. Theoretical simulations indicate that the magnetization curve can be slightly different near the critical temperature for samples with different demagnetization factors [7]. It could be an explanation of the discrepancy within the two curves, but it is difficult to extract such detailed conclusions as the histogram method, only gives an approximate value.

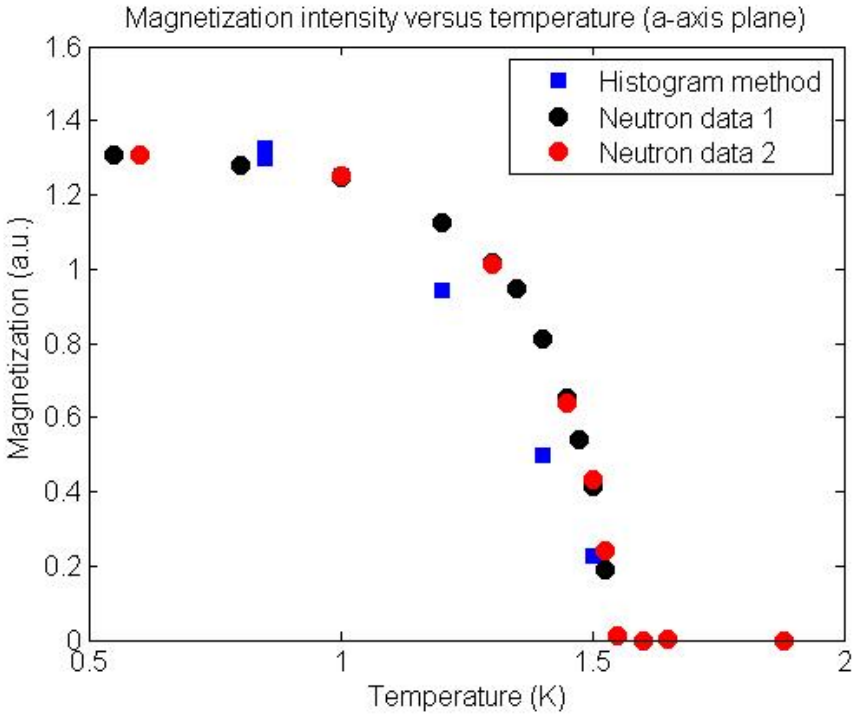

Figure 4.8: Magnetization *versus* temperature extracted from fitting the histograms obtained form the a-c plane SHPM images of the cubic sample, compared to experimental data obtained with neutron diffraction.

Finally, it would be interesting to make a small theoretical extrapolation to be able to relate the signal read by the HP to a meaningful quantitative surface magnetization. For that, one should obviously first check that the hall probe is correctly calibrated, by applying a small field with the electomagnet when we are at dilution temperatures. Special attention should be given to the interpretation of the a-c plane images, as the understanding of the observed magnetic field near the surface is not straightforward. To have better magnetization curves we also could, after performing a SHPM image to locate the different domains, leave the HP in a certain position with the STM feedback on, and ramp one of the order parameters as we measure the Hall signal. This is a dangerous operation, as the sample can move with due to magnetic torques or thermal expansion. It is worth to take the risk of damaging a HP as it would give very good quantitative measurements.

Conclusion

We have described an experimental setup that allows us to perform SHPM imaging at ultra low temperature. The SHPM has been modified in order to overcome design limitations which resulted in an inadequate thermal conductivity between the sample and the MC. There are still some technical problems that have to be improved, as the high field performance. Nevertheless, this thesis shows some of the outstanding information we can get from this technique.

The magnetic domain structure of $LiHoF_4$ has been shown to be of cylinder-like domains along the c-axis. These cylinders are believed to be organized in a regular lattice, their size is in the order of few microns, and seems to depend on the sample geometry. Their shape is strongly deformed by an underlying structure that may correspond to branched states near the surface. An image was successfully taken during the ferromagnetic phase transition, this open the door to a direct study of phase transition, by observing the change in the order parameter in real space.

The dynamics of the domain walls when changing either the temperature or the transverse field resulted to be of great interest. As we increase the temperature, the domain structure seems to not change on the a-a plane surface, whereas in the a-c plane some significant changes are visible when getting close to the transition temperature. This observation could suggest, that close to the transition temperature there is an extension of the branched states through the crystal. When applying a transverse field, the domains increase their size very easily, suggesting an unpinning of the domain walls. We also shown that the size of the domain structure doesn't depend only on the field and temperature conditions, but also on the path in the phase diagram that was used to get there.

An appropriate mathematical treatment of the images, similar to two dimensional deconvolution, should enhance the image resolution. This could eventually help to enlighten some discussions, such as the broadening of domain walls when applying a transverse field, or the proliferation of branched states. Finally we presented a method capable of tracking the changes in magnetization with temperature in a meaningful way. We compared these measurements, with experimental results obtained with neutron diffraction, and found good agreement.

This work aspires to be able to bring some answers that lead to the development of a theory of magnetic domains for $LiHoF_4$, and other dipolar magnets, that correctly matches experiments. It also outlines possible directions of study to be able to overcome the present limitations of the current implementation of this experimental technique.

Bibliography

[1] Gerd Binning, Heinrich Rohrer, Ch Gerber, and E Weibel. Surface studies by scanning tunneling microscopy. *Physical Review Letters*, 49(1):57–61, 1982.

[2] AM Chang, HD Hallen, L Harriott, HF Hess, HL Kao, J Kwo, RE Miller, R Wolfe, J Van der Ziel, and TY Chang. Scanning hall probe microscopy. *Applied physics letters*, 61(16):1974–1976, 1992.

[3] PE Hansen, Torben Johansson, and Rolf Nevald. Magnetic properties of lithium rare-earth fluorides: Ferromagnetism in lierf_ {4} and lihof_ {4} and crystal-field parameters at the rare-earth and li sites. *Physical Review B*, 12(11):5315, 1975.

[4] D Bitko, TF Rosenbaum, and G Aeppli. Quantum critical behavior for a model magnet. *Physical review letters*, 77(5):940, 1996.

[5] Julian Piatek. *Ultra Low Temperature Susceptometer and Magnetometer Study of the Spin Glass Series* $LiHo_xEr_{1-x}F_4$. PhD thesis, EPFL, 2012.

[6] HM Rønnow, Jens Jensen, R Parthasarathy, G Aeppli, TF Rosenbaum, DF McMorrow, and C Kraemer. Magnetic excitations near the quantum phase transition in the ising ferromagnet lihof_ {4}. *Physical Review B*, 75(5):054426, 2007.

[7] Anders Biltmo and Patrik Henelius. The ferromagnetic transition and domain structure in lihof4. *EPL (Europhysics Letters)*, 87(2):27007, 2009.

[8] M Gabay and T Garel. Phase transitions and size effects in the ising dipolar magnet. *Journal de physique*, 46(1):5–16, 1985.

[9] M Gabay and T Garel. Properties of the branched state of an ising dipolar magnet. *Journal de Physique Lettres*, 45(20):989–997, 1984.

[10] JE Battison, A Kasten, MJM Leask, JB Lowry, and BM Wanklyn. Ferromagnetism in lithium holmium fluoride-lihof4. ii. optical and spectroscopic measurements. *Journal of Physics C: Solid State Physics*, 8(23):4089, 1975.

[11] Peter Meyer, Jacques Pommier, and Jacques Ferre. Magnetooptic observation of domains at low temperature in the transparent ferromagnet lihof [sub] 4 [/sub]. In *1989 Intl Congress on Optical Science and Engineering*, pages 93–98. International Society for Optics and Photonics, 1989.

[12] DM Silevitch, G Aeppli, and TF Rosenbaum. Switchable hardening of a ferromagnet at fixed temperature. *Proceedings of the National Academy of Sciences*, 107(7):2797–2800, 2010.

[13] J Brooke, D Bitko, G Aeppli, et al. Quantum annealing of a disordered magnet. *Science*, 284(5415):779–781, 1999.

[14] Hiroshi Fukuyama, Hiroki Tan, Tetsuya Handa, Tomohisa Kumakura, and Masashi Morishita. Construction of an ultra-low temperature scanning tunneling microscope. *Czechoslovak Journal of Physics*, 46(5):2847–2848, 1996.

[15] Craig N and Lester T. Hitchhikers guide to the dilution refrigerator, 2004.

[16] G Frossati. Obtaining ultralow temperatures by dilution of 3he into 4he. *Le Journal de Physique Colloques*, 39(C6):C6–1578, 1978.

[17] FrankPobell. *Matter and Methods at Low Temperatures*. Springer, 2007.

[18] Du-Xing Chen, Enric Padro, and Alvaro Sanchez. Demagnetizing factors of rectangular prisms and ellipsoids. *Magnetics, IEEE transactions on*, 38(4):1742–1752, 2002.

[19] Du-Xing Chen, James A Brug, and Ronald B Goldfarb. Demagnetizing factors for cylinders. *Magnetics, IEEE Transactions on*, 27(4):3601–3619, 1991.

[20] RI Joseph and E Schlomann. Demagnetizing field in nonellipsoidal bodies. *Journal of Applied Physics*, 36(5):1579–1593, 1965.

[21] AH Cooke, DA Jones, JFA Silva, and MR Wells. Ferromagnetism in lithium holmium fluoride-lihof4. i. magnetic measurements. *Journal of Physics C: Solid State Physics*, 8(23):4083, 1975.